Covariant density functional theory for magnetic rotation

J. Peng (彭婧),[1,2,3] J. Meng (孟杰),[2,4,5,*] P. Ring,[3,6,†] and S. Q. Zhang (张双全)[2]

[1]*Department of Physics, Beijing Normal University, Beijing 100875, People's Republic of China*

[2]*School of Physics, Peking University, Beijing 100871, People's Republic of China*

[3]*Physik Department, Technische Universität München, D-85747 Garching, Germany*

[4]*Institute of Theoretical Physics, Chinese Academy of Science, Beijing 100080, People's Republic of China*

[5]*Center of Theoretical Nuclear Physics, National Laboratory of Heavy Ion Accelerator, Lanzhou 730000, People's Republic of China*

[6]*Departamento de Física Teórica, Universidad Autónoma de Madrid, E-28049 Madrid, Spain*

(Received 5 December 2007; published 25 August 2008)

The tilted axis cranking formalism is implemented in relativistic mean field (RMF) theory. It is used for a microscopic description of magnetic rotation in the framework of covariant density functional theory. We assume that the rotational axis is in the xz plane and consider systems with the two symmetries $\mathcal{P}$ (space reflection) and $\mathcal{P}_y\mathcal{T}$ (a combination of a reflection in the y direction and time reversal). A computer code based on these symmetries is developed, and first applications are discussed for the nucleus ^{142}Gd: the rotational band based on the configuration $\pi h_{11/2}^2 \otimes \nu h_{11/2}^{-2}$ is investigated in a fully microscopic and self-consistent way. The results are compared with available data, such as spectra and electromagnetic transition ratios $B(M1)/B(E2)$. The relation between rotational velocity and angular momentum are discussed in detail together with the shears mechanism characteristic of magnetic rotation.

DOI: 10.1103/PhysRevC.78.024313 PACS number(s): 21.60.Jz, 21.10.−k, 23.20.−g, 27.60.+j

I. INTRODUCTION

The study of bands with high angular momenta has been at the forefront of nuclear structure physics for many years. Many exciting phenomena have been discovered and predicted, such as Coriolis antipairing [1], backbending [2], alignment phenomena [3,4], rotating giant resonances [5], superdeformed rotational bands [6], magnetic rotation [7], wobbling motion [8], and chiral phenomena [9].

Many of these phenomena were first discussed in phenomenological models such as the particle plus rotor model [8]. For a microscopic understanding, the semiphenomenological Cranking model [10] has been used with great success. Because of the high complexity of these phenomena, where collective degrees of freedom such as deformation and superfluidity connected with symmetry violations and phase transitions in the mesoscopic nuclear system have a strong interplay with single-particle configurations based on orbitals with high single-particle angular momentum, fully quantum mechanical many-body calculations are even today beyond the computational possibilities. Only in very light systems has the shell model been applied [11], and it has been found that cranked Hartree-Fock-Bogoliubov (HFB) theory provides a very successful method for a self-consistent and fully microscopic description of these complex phenomena. It has also been shown that the cranking approximation can be understood as an approximate angular momentum projection before the variation [12]. Most of the applications of cranking theory are based on principal axis cranking (PAC), also called *one-dimensional cranking*, where the rotational axis is parallel to one of the principal axes of the deformed nucleus, usually parallel to the x axis and perpendicular to the symmetry axis of the system, usually the z axis.

Cranking calculations are three-dimensional calculations and therefore highly complex. Most of the applications are therefore based on simple model Hamiltonians, such as the pairing-plus-quadrupole model [13] or on microscopic-macroscopic (mic-mac) models such as the Nilsson-Strutinsky method in the rotating frame [14]. Even today many of the investigations are carried out in such semiphenomenological models. Fully self-consistent calculations based on universal density functionals such as Skyrme [15] or Gogny [16] or on relativistic density functionals [17,18] are relatively rare.

The term "magnetic rotation" has been attributed to the so-called shears bands, which have strong $M1$ transitions and very weak $E2$ transitions. They were experimentally observed in the region of proton-rich Pb isotopes during the 1990s [19–28]. The description of the shears bands requires a model that goes beyond principal axis cranking. In other words, the rotating axis does not coincide with any principal axis of the atomic nucleus. This leads to the tilted axis cranking (TAC) model [29], which has been used for the interpretation of the magnetic rotation [7].

Shears bands are based on relatively few high-j orbitals of protons and neutrons close to a nearly spherical core with different particle-hole (p-h) structure. Configurations with maximally aligned single-particle angular momentum have an oblate density distribution for particles and a prolate density distribution for holes. In the following, we discuss a configuration of high-j proton particles and high-j neutron holes. Of course configurations with proton holes and neutron particles lead to the same effects. At the band head, the neutron holes have angular momenta $\mathbf{J}_n$ aligned in the direction of the z axis producing in this way an prolate density distribution. The proton particles have an oblate density distribution. To maximize the overlap of the orbits in this configuration, at the

*mengj@pku.edu.cn
†ring@ph.tum.de

band head, the angular momenta $\mathbf{J}_p$ of the proton particles point in a direction almost orthogonal to the neutrons, i.e., in the direction of the x axis. This coupling results in a total angular momentum $\mathbf{J} = \mathbf{J}_p + \mathbf{J}_n$ tilted from the principal axes and pointing in the xz plane. Within the Cranking model, the rotational axis is therefore tilted (TAC) pointing in the xz plane. This is also called *two-dimensional cranking*. The magnetic dipole vector μ arising from these few valence proton and neutron high-j orbitals, rotates around the total angular momentum vector $\mathbf{J}$. With increasing rotational frequency, both the proton and neutron angular momenta align toward the total angular momentum. Consequently, in the intrinsic frame, the direction of the total angular momentum does not change much, and regular rotational bands are formed even though the total density distribution of the nucleus is almost spherical or weakly deformed. Therefore this kind of rotation has been called *magnetic rotation* in order to distinguish it from the usual collective rotation in well-deformed nuclei (called *electric rotation*) [7]. Collective rotations in a finite many-body system such as the nucleus are only possible for configurations with a well-defined orientation and small fluctuations around it, i.e., with a strong violation of symmetry in the intrinsic frame [30]. Conventional collective rotations are based on a strong deformation of the density distribution with a symmetry axis in the z direction, leading to strong $E2$ transitions. Magnetic rotation occurs in systems with small deformation of the density distribution. The orientation and therefore the symmetry violation are determined by the currents of the valence neutrons and protons, leading to strong $M1$ transitions.

The magnetic properties for the shears bands in ^{199}Pb were investigated experimentally in 1994 by lifetime measurements [25]. The deduced $B(M1)$ values are roughly twice those predicted by the TAC model and show a different behavior with the rotational frequency. Later experimental lifetime measurements by Clark *et al*. for four $M1$ bands in ^{198,199}Pb in 1997 [27] found better agreement with the TAC calculations and provided a clear evidence for magnetic rotation. To date, more than 130 magnetic dipole bands have been identified for 61 nuclides in four mass regions: $A \sim 80$ (Br, Kr, Rb, Zr), $A \sim 100$ (Ag, Cd, In, Sn, Sb, Te), $A \sim 130$ (Xe, Ba, La, Ce, Pr, Nd, Sm, Eu, Gd), and $A \sim 200$ (Hg, Pb, Bi, Rn) [31]. The magnetic rotations for these regions correspond to different configurations of high-j valence nucleons, e.g., $\pi g_{9/2}$ particles combined with $\nu g_{9/2}$ holes for the $A \sim 80$ region, $\pi g_{9/2}$ holes with $\nu h_{11/2}$ particles for $A \sim 100$, $\pi h_{11/2}$ particles with $\nu h_{11/2}$ holes for $A \sim 130$, $\pi i_{13/2}$ particles with $\nu i_{13/2}$ holes for $A \sim 200$, etc.

The magnetic rotation occurs because the axis of the uniform rotation does not coincide with any principal axis of the density distribution. Theoretically, the semiclassical mean field description for tilted axis rotation can be traced back to the 1980s [32,33]. The qualities of the TAC approximation were discussed and tested in Ref. [34] with the particle plus rotor model (PRM) which also has led to a remarkably successful description of chiral doublet bands [9,35,36], where the angular momentum points in an arbitrary direction, also called *three-dimensional cranking*. A review of the tilted axis cranking approach can be found in Ref. [29]. All these investigations have been carried out in simple models such as the particle plus rotor model or non-self-consistent cranking models with a few high-j orbitals in a fixed deformed mean field. Only recently, relativistic [37] and nonrelativistic [38,39] density functionals have been used for fully microscopic investigations of magnetic rotation and of chiral doublet bands.

For many years, density functional theory based on the mean field approach has played an important role in a fully microscopic and universal description of medium-heavy and heavy nuclei. In principle, such theories can provide an exact description of the many-body dynamics, if the exact density functional is known; but for such systems as nuclei, one is far from a microscopic derivation of this functional. The most successful descriptions are based on density functionals depending on phenomenological parameters adjusted to a few finite nuclei distributed all over the periodic system. Covariant density functional theory (CDFT) is particularly successful, because Lorentz invariance reduces the number of parameters considerably. It is based on the Walecka model [40], which was originally considered as a fully fledged quantum field theory of the nucleus [41]. However, the real breakthrough making quantitative applications of high precision possible occurred when Boguta and Bodmer [42] discovered that an additional density dependence was necessary. Therefore, today the relativistic mean field theory with an additional density dependence is considered a covariant density functional approach [43]. It has been extended to include pairing correlations in the framework of relativistic Hartree-Bogoliubov (RHB) theory in Refs. [44–47].

During the past two decades, CDFT has received wide attention, and several review articles have appeared [48–53]. With a relatively small number of parameters which are adjusted to reproduce global properties of spherical closed-shell nuclei, a large variety of nuclear phenomena have been described over the years within this kind of model: ground state properties of finite spherical and deformed nuclei all over the periodic table [54] from light nuclei [55] to super-heavy elements [56,57], from the neutron drip line, where halo phenomena are observed [58] and new giant halos are predicted [59], to the proton drip line [60] with nuclei unstable against the emission of protons [61]. In addition, this theory gives a natural explanation for the origin of pseudospin symmetry—a long-existing mystery in nuclear physics [62–69].

Starting from the time-dependent version of CDFT, the same functionals can also be applied to the description of excited states. In the small amplitude limit, one finds the relativistic random-phase approximation (RRPA) [70] and quasiparticle RRPA [71] for the description of excited states with vibrational character, in particular, for the description of the positions of giant resonances and spin- or/and isospin-excitations as the Gamov-Teller resonance (GTR) or the isobaric analog resonance (IAR) [72]. Recently, they have been also used for a theoretical interpretation of low-lying dipole [71] and quadrupole [73,74] excitations and for the scissor modes in deformed nuclei [75].

On the basis of the same functionals and without any additional phenomenological parameters, rotational excitations can be described in the framework of the relativistic cranking model [76]. These calculations provide an excellent

description of superdeformed bands [17,18] and a new mechanism for the interpretation of identical bands in superdeformed nuclei [77]. Multiple chiral doublets based on triaxial deformation and the corresponding configuration have been investigated in Ref. [78]. Although the cranked RMF equations with arbitrary orientation of the angular momentum vector (three-dimensional cranking) have been developed since 2000, because of their numerical complexity, they have so far been applied to only one band of magnetic rotation in the nucleus ^{84}Rb [37].

In this investigation, the self-consistent tilted axis cranking RMF approach is applied to the investigation of bands based on magnetic rotation. A completely new computer code for self-consistent relativistic tilted axis cranking has been developed. It includes considerable improvements, and by using the technologies of modern supercomputers it allows general systematic investigations of such bands. In Sec. II we present the equations of relativistic tilted axis cranking. In Sec. III we discuss essential numerical details, and in Sec. IV we present, as an example, results for the band DB1 in ^{142}Gd, which is based on the configuration $\pi h_{11/2}^2 \otimes \nu h_{11/2}^{-2}$. In particular, we discuss the spectrum, the electromagnetic transition ratio $B(M1)/B(E2)$, the relation between the rotational frequency and the angular momentum, and the characteristics of magnetic rotation and the shears mechanism. In Sec. V we summarize our results.

II. RELATIVISTIC TILTED AXIS CRANKING THEORY

The starting point of covariant density functional theory is the standard effective Lagrangian density constructed with the degrees of freedom associated with the nucleon field ψ, the two isoscalar meson fields σ and ω, the isovector meson field ρ, and the photon field A [41,48,49,52,53]:

$$\begin{aligned}\mathcal{L} = \bar{\psi}\Big[& i\gamma^\mu\partial_\mu - m - g_\sigma\sigma - g_\omega\gamma^\mu\omega_\mu - g_\rho\gamma^\mu\vec{\tau}\cdot\vec{\rho}_\mu \\ & - e\gamma^\mu\frac{1-\tau_3}{2}A_\mu\Big]\psi \\ & + \frac{1}{2}\partial^\mu\sigma\,\partial_\mu\sigma - \frac{1}{2}m_\sigma^2\sigma^2 - \frac{1}{3}g_2\sigma^3 - \frac{1}{4}g_3\sigma^4 \\ & - \frac{1}{4}\Omega_{\mu\nu}\Omega^{\mu\nu} + \frac{1}{2}m_\omega^2\omega_\mu\omega^\mu + \frac{1}{4}c_3(\omega_\mu\omega^\mu)^2 \\ & - \frac{1}{4}\vec{R}_{\mu\nu}\vec{R}^{\mu\nu} + \frac{1}{2}m_\rho^2\vec{\rho}_\mu\vec{\rho}^\mu - \frac{1}{4}F_{\mu\nu}F^{\mu\nu}, \end{aligned} \tag{1}$$

where the field tensors for the vector mesons and the photon are defined as

$$\begin{aligned}\Omega_{\mu\nu} &\equiv \partial_\mu\omega_\nu - \partial_\nu\omega_\mu, \\ \vec{R}_{\mu\nu} &\equiv \partial_\mu\vec{\rho}_\nu - \partial_\nu\vec{\rho}_\mu, \\ F_{\mu\nu} &\equiv \partial_\mu A_\nu - \partial_\nu A_\mu. \end{aligned} \tag{2}$$

The Lagrangian (1) also includes nonlinear self-couplings of the σ meson and the ω meson characterized by the parameters g_2, g_3, and c_3. In this paper, arrows are used to indicate vectors in isospin space, and boldface characters are used for the vectors in r space.

To describe magnetic rotation, we assume that the nucleus rotates around an axis in the xz plane. The Lagrangian in Eq. (1) is transformed to the frame rotating with the uniform velocity

$$\boldsymbol{\Omega} = (\Omega_x, 0, \Omega_z) = (\Omega\cos\theta_\Omega, 0, \Omega\sin\theta_\Omega), \tag{3}$$

where $\theta_\Omega := \sphericalangle(\boldsymbol{\Omega}, \mathbf{e}_x)$ is the angle between the rotational axis and the x axis. According to Ref. [79], the equations of motion can be obtained from the Lagrangian in the rotating frame as

$$[\boldsymbol{\alpha}(-i\nabla - \mathbf{V}) + \beta(m + S) + V - \boldsymbol{\Omega}\hat{\mathbf{J}}]\psi_i = \varepsilon_i\psi_i, \tag{4}$$

where $\hat{\mathbf{J}} = \hat{\mathbf{L}} + \frac{1}{2}\hat{\boldsymbol{\Sigma}}$ is the total angular momentum of the nucleon spinors, and the relativistic fields $S(\mathbf{r})$, $V^\mu(\mathbf{r})$ are given in terms of the meson fields:

$$\begin{aligned} S(\mathbf{r}) &= g_\sigma\sigma(\mathbf{r}), \\ V(\mathbf{r}) &= g_\omega\omega_0(\mathbf{r}) + g_\rho\tau_3\rho_{30}(\mathbf{r}) + e\frac{1-\tau_3}{2}A_0(\mathbf{r}), \\ \mathbf{V}(\mathbf{r}) &= g_\omega\boldsymbol{\omega}(\mathbf{r}) + g_\rho\tau_3\boldsymbol{\rho}_3(\mathbf{r}) + e\frac{1-\tau_3}{2}\mathbf{A}(\mathbf{r}). \end{aligned} \tag{5}$$

The meson fields and the electromagnetic field obey the equations of motion

$$\begin{aligned} \left[-\Delta + m_\sigma^2 - (\boldsymbol{\Omega}\hat{\mathbf{L}})^2\right]\sigma &= -g_\sigma\rho_s - g_2\sigma^2 - g_3\sigma^3, \\ \left[-\Delta + m_\omega^2 - (\boldsymbol{\Omega}\hat{\mathbf{L}})^2\right]\omega^0 &= g_\omega\rho_v - c_3(\omega^\nu\omega_\nu)\omega^0, \\ \left[-\Delta + m_\omega^2 - (\boldsymbol{\Omega}(\hat{\mathbf{L}} + \hat{\mathbf{S}}))^2\right]\boldsymbol{\omega} &= g_\omega\mathbf{j}_v - c_3(\omega^\nu\omega_\nu)\boldsymbol{\Omega}, \\ \left[-\Delta + m_\rho^2 - (\boldsymbol{\Omega}\hat{\mathbf{L}})^2\right]\rho_{30} &= g_\rho\rho_3, \\ \left[-\Delta + m_\rho^2 - (\boldsymbol{\Omega}(\hat{\mathbf{L}} + \hat{\mathbf{S}}))^2\right]\boldsymbol{\rho}_3 &= g_\rho\mathbf{j}_3, \\ [-\Delta - (\boldsymbol{\Omega}\hat{\mathbf{L}})^2]A_0 &= e\rho_c, \\ [-\Delta - (\boldsymbol{\Omega}(\hat{\mathbf{L}} + \hat{\mathbf{S}}))^2]\mathbf{A} &= e\mathbf{j}_c. \end{aligned} \tag{6}$$

As usual, we neglect the Coriolis terms $(\boldsymbol{\Omega}\hat{\mathbf{L}})^2$ and $(\boldsymbol{\Omega}(\hat{\mathbf{L}} + \hat{\mathbf{S}}))^2$ for the meson fields. As discussed in Refs. [76,79], these contributions are extremely small, because they are quadratic in the rotational frequency and because the mesons are bosons sitting to a large part in s-states, i.e., nearly all the angular momentum comes from the fermions. Since the coupling constant of the electromagnetic interaction is small compared with the coupling constants of the meson fields, the spatial components of the vector potential $\mathbf{A}(\mathbf{r})$ are neglected in our investigations.

Since the Coriolis terms in the Dirac equation (4) break time-reversal symmetry in the intrinsic frame, spatial components of the currents are induced. The densities and currents entering the source terms in Eq. (6) have the form

$$\begin{aligned} \rho_s(\mathbf{r}) &= \sum_i^A \overline{\psi}_i(\mathbf{r})\psi_i(\mathbf{r}), \\ \rho_v(\mathbf{r}) &= \sum_i^A \psi_i^\dagger(\mathbf{r})\psi_i(\mathbf{r}), \\ \mathbf{j}_v(\mathbf{r}) &= \sum_i^A \psi_i^\dagger(\mathbf{r})\boldsymbol{\alpha}\psi_i(\mathbf{r}), \end{aligned}$$

$$\rho_3(\mathbf{r}) = \sum_i^A \psi_i^\dagger(\mathbf{r})\tau_3\psi_i(\mathbf{r}), \tag{7}$$

$$\mathbf{j}_3(\mathbf{r}) = \sum_i^A \psi_i^\dagger(\mathbf{r})\boldsymbol{\alpha}\tau_3\psi_i(\mathbf{r}),$$

$$\rho_c(\mathbf{r}) = \sum_i^A \psi_i^\dagger(\mathbf{r})\frac{1-\tau_3}{2}\psi_i(\mathbf{r}),$$

$$\mathbf{j}_c(\mathbf{r}) = \sum_i^A \psi_i^\dagger(\mathbf{r})\boldsymbol{\alpha}\frac{1-\tau_3}{2}\psi_i(\mathbf{r}).$$

The sums are taken over the particle states only, i.e., the contributions of the negative-energy states are neglected (the no-sea approximation).

The total energy in the laboratory frame is given by

$$\begin{aligned} E = &\sum_i^A \varepsilon_i + E_{\text{c.m.}} - \frac{1}{2}\int d^3r \left(g_\sigma\sigma\rho_s + \frac{1}{3}g_2\sigma^3 + \frac{1}{2}g_3\sigma^4\right) \\ &- \frac{1}{2}\int d^3r \left[g_\omega(\omega_0\rho_\upsilon - \boldsymbol{\omega}\mathbf{j}_\upsilon) - \frac{1}{2}c_3(\omega_\nu\omega^\nu)^2\right] \\ &- \frac{1}{2}\int d^3r g_\rho[\rho_{30}\rho_3 - \boldsymbol{\rho}_3\mathbf{j}_3] \\ &- \frac{1}{2}\int d^3r eA_0\rho_c + \sum_i^A \langle i|\boldsymbol{\Omega}\hat{\mathbf{J}}|i\rangle \\ &+ \int d^3r\{\sigma(\boldsymbol{\Omega}\hat{\mathbf{L}})^2\sigma - \omega_0(\boldsymbol{\Omega}\hat{\mathbf{L}})^2\omega_0 - \rho_{30}(\boldsymbol{\Omega}\hat{\mathbf{L}})^2\rho_{30} \\ &+ \boldsymbol{\omega}[\boldsymbol{\Omega}(\hat{\mathbf{L}}+\hat{\mathbf{S}})]^2\boldsymbol{\omega} + \boldsymbol{\rho}_3[\boldsymbol{\Omega}(\hat{\mathbf{L}}+\hat{\mathbf{S}})]^2\boldsymbol{\rho}_3\}, \end{aligned} \tag{8}$$

where $E_{\text{c.m.}} = -\langle\mathbf{P}^2\rangle/2M$ is the correction for the spurious center-of-mass motion. Following the standard techniques, the root-mean-square (rms) radius of the system is defined as

$$\langle r^2\rangle^{1/2} = \left[\frac{\int d^3r r^2\rho(\mathbf{r})}{\int d^3r\rho(\mathbf{r})}\right]^{1/2}. \tag{9}$$

From the expectation values of the angular momenta

$$\begin{aligned} J_x = \langle\hat{J}_x\rangle = \left\langle\sum_{i=1}^A \hat{j}_x^{(i)}\right\rangle, \qquad J_y = 0, \\ J_z = \langle\hat{J}_z\rangle = \left\langle\sum_{i=1}^A \hat{j}_z^{(i)}\right\rangle, \end{aligned} \tag{10}$$

and using the cranking condition, we find the total angular momentum

$$J = \sqrt{\langle\hat{J}_x\rangle^2 + \langle\hat{J}_z\rangle^2} \equiv \sqrt{I(I+1)}. \tag{11}$$

The orientation of the angular momentum vector

$$\mathbf{J} = (\langle\hat{J}_x\rangle, 0, \langle\hat{J}_z\rangle) = (J\cos\theta_J, 0, J\sin\theta_J) \tag{12}$$

is given by the angle $\theta_J := \sphericalangle(\mathbf{J}, \mathbf{e}_x)$ between the angular momentum vector $\mathbf{J}$ and the x axis. Since we minimize $\langle\hat{H} - \hat{\mathbf{J}}\Omega\rangle$ and since $\langle\hat{\mathbf{J}}\Omega\rangle$ is maximal for $\mathbf{J} \parallel \boldsymbol{\Omega}$, the orientation θ_J of the average angular momentum $\mathbf{J}$ should be identical to the orientation $\theta_\Omega = \sphericalangle(\boldsymbol{\Omega}, \mathbf{e}_x)$ of the angular velocity $\boldsymbol{\Omega}$, i.e., $\theta_J = \theta_\Omega$, for the self-consistent solution without constraint.

The quadrupole moments $\mathcal{Q}_{20}$ and $\mathcal{Q}_{22}$ are calculated in the same way by

$$\mathcal{Q}_{20} = \sqrt{\frac{5}{16\pi}}\langle 3z^2 - r^2\rangle, \qquad \mathcal{Q}_{22} = \sqrt{\frac{15}{32\pi}}\langle x^2 - y^2\rangle. \tag{13}$$

From the quadrupole moments

$$\mathcal{Q}_{20} = \frac{3A}{4\pi}R_0^2 a_{20}, \qquad \mathcal{Q}_{22} = \frac{3A}{4\pi}R_0^2 a_{22}, \tag{14}$$

the deformation parameters a_{20}, a_{22} and β, γ can be extracted as

$$\beta = \sqrt{a_{20}^2 + 2a_{22}^2}, \qquad \gamma = \arctan\left[\sqrt{2}\frac{a_{22}}{a_{20}}\right], \tag{15}$$

with $R_0 = 1.2A^{1/3}$ fm. Note, that we use in this work the sign convention of Ref. [30] for the definition of γ.

In the usual PAC programs (one-dimensional cranking), the principal axes of the densities and fields are implemented to be along the x, y, and z axis. The TAC code used in this investigation (two-dimensional cranking) allows for arbitrary rotations of the density distributions around the intrinsic y axis, i.e., only one of the principal axes of the densities and fields is oriented along the y axis. Otherwise, the density can have an arbitrary orientation in the xz plane. Of course, this is a restriction compared to the freedom for general rotations around all three axes, as it is needed in the case of chiral rotations (three-dimensional cranking). Keeping the y axis fixed has the numerical advantage that for the conventional choice of phases in Ref. [80], the matrix elements of the rotational matrices $d^j_{mm'}$ describing rotations around the y axis are real. The freedom of rotations around the y axis can lead (in particular for $\Omega = 0$ and small Ω values) to instabilities during the iterative solution, because the solutions with different orientations in the xz plane are degenerate. We therefore enforce the principal axes of the density distribution to be identical with the x, y, and z axis by introducing a quadratic constraint [30] for the expectation value of the quadrupole moment

$$\langle\hat{\mathcal{Q}}_{2-1}\rangle = -\sqrt{\frac{15}{8\pi}}\langle xz\rangle = 0, \tag{16}$$

i.e., by minimizing

$$\langle H'\rangle = \langle H\rangle + \tfrac{1}{2}C(\langle\hat{\mathcal{Q}}_{2-1}\rangle - a_{2-1})^2, \tag{17}$$

with $a_{2-1} = 0$. C is a spring constant, which, if properly chosen, has no influence on the final result. Of course, this additional constraint should, in principle, not be necessary for Ω different from zero, because the axis of rotation determines an orientation and lifts this degeneracy with respect to rotations around the y axis in this case. However, if one wants to investigate the energy surface as a function of the orientation of the rotational axis $\boldsymbol{\Omega}$ in the xz plane determined by the angle θ_Ω between the direction of $\boldsymbol{\Omega}$ and the principal axis of the density distribution, it is necessary to keep the orientation of the density distribution fixed. As we shall see, the energy surface is rather flat as a function of the rotational angle θ_Ω.

This leads to a high degree of instability during the iteration, and it is advisable to keep the orientation θ_Ω fixed during the iterative solution. Of course, for a fully self-consistent solution, θ_Ω cannot be kept fixed arbitrarily. The optimal value for θ_Ω has been determined by solving the equations for various values of θ_Ω and by minimizing the Routhian afterward with respect to θ_Ω.

The nuclear magnetic moment is given by [81]

$$\boldsymbol{\mu} = \sum_i^A \int d^3r \left[\frac{mc^2}{\hbar c} q_i \psi_i^\dagger(\mathbf{r}) \mathbf{r} \times \boldsymbol{\alpha} \psi_i(\mathbf{r}) + \kappa_i \psi_i^\dagger(\mathbf{r}) \beta \boldsymbol{\Sigma} \psi_i(\mathbf{r}) \right], \tag{18}$$

where q is the charge ($q_p = 1$ for protons and $q_n = 0$ for neutrons), m the nucleon mass, and κ the free anomalous gyromagnetic ratio of the nucleon ($\kappa_p = 1.793$ and $\kappa_n = -1.913$).

From the quadrupole moments and the magnetic moment, the $B(M1)$ and $B(E2)$ transition probabilities can be derived in semiclassical approximation [9]

$$B(M1) = \frac{3}{8\pi} (\mu_x \sin\theta_J - \mu_z \cos\theta_J)^2, \tag{19}$$

$$B(E2) = \frac{15}{128\pi} \left[\mathcal{Q}_{20} \cos^2\theta_J + \sqrt{\frac{2}{3}} \mathcal{Q}_{22} (1 + \sin^2\theta_J) \right]^2, \tag{20}$$

where $\theta_J 1 := \sphericalangle(\mathbf{J}, \mathbf{e}_x)$ is determined by the orientation of the average angular momentum in Eq. (12).

III. NUMERICAL DETAILS

A new code for the solution of the tilted axis cranking relativistic mean field equations has been developed. As in the older calculations with principal axis cranking [77], the Dirac spinors are expanded in terms of three-dimensional harmonic oscillator wave functions in Cartesian coordinates, i.e., the dependence on the coordinates $\mathbf{r} = (x, y, z)$ is represented by linear combinations of the product states

$$\varphi_{n_x n_y n_z}(\mathbf{r}) = \langle \mathbf{r} | n_x, n_y, n_z \rangle = \varphi_{n_x}(x) \varphi_{n_y}(y) \varphi_{n_z}(z), \tag{21}$$

where the normalized oscillator function $\varphi_{n_k}(x_k)$ in the k direction ($x_k = x, y, z$) is given by

$$\varphi_{n_k}(x_k) = \frac{N_{n_k}}{\sqrt{b_k}} H_{n_k}\left(\frac{x_k}{b_k}\right) \exp\left[-\frac{1}{2} \left(\frac{x_k}{b_k}\right)^2 \right]. \tag{22}$$

$N_n = (\sqrt{\pi} 2^n n!)^{-1/2}$ is a normalization factor, and

$$H_n(\xi) = (-1)^n e^{\xi^2} \frac{d^n}{d\xi^n} e^{-\xi^2} \tag{23}$$

are the Hermite polynomials [82]. The oscillator length parameters b_k allow for a deformation of the basis with the deformation parameters β_0 and γ_0, which should be close but not necessarily equal to the resulting deformation of the density distribution.

For each combination of quantum numbers (n_x, n_y, n_z), the spin part is chosen in such a way that the basis functions are eigenfunctions of the simplex operator [83] $\mathcal{S} = PR_1$, where $\mathcal{P}$ is the parity and $\mathcal{R}_1$ is the signature operator [84], i.e., a rotation by 180° around the x axis. $\mathcal{S}$ corresponds therefore to an inversion at the yz plane: $(x, y, z) \to (-x, y, z)$ with the eigenvalues $\pm i$ in the space of single fermion wave functions. Using the fact that

$$\mathcal{S} |n_x, n_y, n_z\rangle = (-)^{n_x} |n_x, n_y, n_z\rangle, \tag{24}$$

and that

$$\mathcal{S} |\uparrow\rangle = e^{i\frac{\pi}{2}\sigma_1} |\uparrow\rangle = i |\downarrow\rangle, \tag{25}$$

we obtain the basis functions for the eigenvalue $+i$ of the simplex operator $\mathcal{S}$

$$\begin{aligned} |\alpha\rangle &= i^{n_y} |n_x, n_y, n_z, +i\rangle \\ &= i^{n_y} |n_x, n_y, n_z\rangle \frac{1}{\sqrt{2}} (|\uparrow\rangle - (-1)^{n_x} |\downarrow\rangle). \end{aligned} \tag{26}$$

The phase factor i^{n_y} has been added to have real matrix elements for the Dirac equation [85]. The eigenfunctions of the simplex operation with eigenvalue $-i$ are obtained by the time reversal operation:

$$\begin{aligned} |\bar{\alpha}\rangle &= \mathcal{T} |\alpha\rangle = |n_x, n_y, n_z, -i\rangle \\ &= (-i)^{n_y} |n_x, n_y, n_z\rangle \frac{1}{\sqrt{2}} (-|\downarrow\rangle - (-1)^{n_x} |\uparrow\rangle). \end{aligned} \tag{27}$$

We therefore use the following basis states:

$$\begin{aligned} \varphi_\alpha(\mathbf{r}, s) &= \langle \mathbf{r}, s | \alpha \rangle \\ &= i^{n_y} \varphi_{n_x}(x) \varphi_{n_y}(y) \varphi_{n_z}(z) \frac{1}{\sqrt{2}} \begin{pmatrix} 1 \\ (-1)^{n_x+1} \end{pmatrix}, \end{aligned} \tag{28}$$

and

$$\begin{aligned} \varphi_{\bar{\alpha}}(\mathbf{r}, s) &= \langle \mathbf{r}, s | \bar{\alpha} \rangle \\ &= (-i)^{n_y} \varphi_{n_x}(x) \varphi_{n_y}(y) \varphi_{n_z}(z) \frac{1}{\sqrt{2}} \begin{pmatrix} (-1)^{n_x+1} \\ -1 \end{pmatrix}. \end{aligned} \tag{29}$$

The Dirac spinor for the nucleon has the form

$$\psi_i(\mathbf{r}) = \begin{pmatrix} f_i(\mathbf{r}, s) \\ i g_i(\mathbf{r}, s) \end{pmatrix} \chi_i(t), \tag{30}$$

where $\chi_i(t)$ is the isospin part. In contrast to principal axis cranking calculations, which preserve simplex symmetry [79], this is in general no longer the case for TAC calculations, and therefore the large and small components of the wave function in Eq. (30) have to be written as linear combinations of the sets (28) and (29) with different simplex:

$$\begin{aligned} f_i(\mathbf{r}, s) &= \sum_\alpha f_{\alpha i} |\alpha\rangle + \sum_{\bar{\alpha}} f_{\bar{\alpha} i} |\bar{\alpha}\rangle, \\ g_i(\mathbf{r}, s) &= \sum_{\tilde{\alpha}} g_{\tilde{\alpha} i} |\tilde{\alpha}\rangle + \sum_{\bar{\tilde{\alpha}}} g_{\bar{\tilde{\alpha}} i} |\bar{\tilde{\alpha}}\rangle. \end{aligned} \tag{31}$$

Since the large and small components in the Dirac equation have different parity, the sums in the expansions for the large and the small components have to run over oscillator quantum numbers with even $N = n_x + n_y + n_z$ or odd N, respectively. This is indicated in Eq. (31) by the indices α and $\tilde{\alpha}$.

On this basis, the solution of Dirac equation (4) is obtained by the matrix diagonalization

$$\mathcal{H}\begin{pmatrix} f_{\alpha i} \\ f_{\bar{\alpha} i} \\ g_{\tilde{\alpha} i} \\ g_{\bar{\tilde{\alpha}} i} \end{pmatrix} = \varepsilon_i \begin{pmatrix} f_{\alpha i} \\ f_{\bar{\alpha} i} \\ g_{\tilde{\alpha} i} \\ g_{\bar{\tilde{\alpha}} i} \end{pmatrix}, \tag{32}$$

where the Hamiltonian matrix $\mathcal{H}$ has the form

$$\begin{pmatrix} \langle\alpha|M^* + V - \boldsymbol{\Omega}\hat{\mathbf{J}}|\alpha'\rangle & \langle\alpha|M^* + V - \boldsymbol{\Omega}\hat{\mathbf{J}}|\bar{\alpha}'\rangle & \langle\alpha|\boldsymbol{\sigma}(\boldsymbol{\nabla} - i\mathbf{V})|\tilde{\alpha}'\rangle & \langle\alpha|\boldsymbol{\sigma}(\boldsymbol{\nabla} - i\mathbf{V})|\bar{\tilde{\alpha}}'\rangle \\ \langle\bar{\alpha}|M^* + V - \boldsymbol{\Omega}\hat{\mathbf{J}}|\alpha'\rangle & \langle\bar{\alpha}|M^* + V - \boldsymbol{\Omega}\hat{\mathbf{J}}|\bar{\alpha}'\rangle & \langle\bar{\alpha}|\boldsymbol{\sigma}(\boldsymbol{\nabla} - i\mathbf{V})|\tilde{\alpha}'\rangle & \langle\bar{\alpha}|\boldsymbol{\sigma}(\boldsymbol{\nabla} - i\mathbf{V})|\bar{\tilde{\alpha}}'\rangle \\ \langle\tilde{\alpha}|-\boldsymbol{\sigma}(\boldsymbol{\nabla} - i\mathbf{V})|\alpha'\rangle & \langle\tilde{\alpha}|-\boldsymbol{\sigma}(\boldsymbol{\nabla} - i\mathbf{V})|\bar{\alpha}'\rangle & \langle\tilde{\alpha}|-M^* + V - \boldsymbol{\Omega}\hat{\mathbf{J}}|\tilde{\alpha}'\rangle & \langle\tilde{\alpha}|-M^* + V - \boldsymbol{\Omega}\hat{\mathbf{J}}|\bar{\tilde{\alpha}}'\rangle \\ \langle\bar{\tilde{\alpha}}|-\boldsymbol{\sigma}(\boldsymbol{\nabla} - i\mathbf{V})|\alpha'\rangle & \langle\bar{\tilde{\alpha}}|-\boldsymbol{\sigma}(\boldsymbol{\nabla} - i\mathbf{V})|\bar{\alpha}'\rangle & \langle\bar{\tilde{\alpha}}|-M^* + V - \boldsymbol{\Omega}\hat{\mathbf{J}}|\tilde{\alpha}'\rangle & \langle\bar{\tilde{\alpha}}|-M^* + V - \boldsymbol{\Omega}\hat{\mathbf{J}}|\bar{\tilde{\alpha}}'\rangle \end{pmatrix}. \tag{33}$$

Note that the Coriolis term $\boldsymbol{\Omega}\hat{\mathbf{J}}$ breaks the invariance with respect to time reversal and with respect to rotations around the x axis as well as around the z axis. Therefore only the invariance of space reflection $\mathcal{P}$ and the combination of time reversal and reflection in y direction $\mathcal{P}_y\mathcal{T}$ are valid and used in the code.

The Klein-Gordon equations for the meson fields (6) are also solved by expanding the meson fields $\phi^{(m)}(\mathbf{r}) = \sigma(\mathbf{r})$, $\omega^{\mu}(\mathbf{r})$, $\rho_3^{\mu}(\mathbf{r})$ in a three-dimensional harmonic oscillator basis with the same oscillator length parameters b_k, and therefore with the same deformation parameters β_0 and γ_0, as the basis of the spinors (21), that is,

$$\phi^{(m)}(\mathbf{r}) = \sum_{n_x n_y n_z} \phi^{(m)}_{n_x n_y n_z} \varphi_{n_x}(x)\varphi_{n_y}(y)\varphi_{n_z}(z), \tag{34}$$

for $m = \sigma, \omega, \rho$. Since the Coriolis terms $(\boldsymbol{\Omega}\hat{\mathbf{L}})^2$ and $(\boldsymbol{\Omega}(\hat{\mathbf{L}} + \hat{\mathbf{S}}))^2$ for the mesons are neglected in the Klein-Gordon equations (6), the corresponding equations of motion for the meson fields become a set of inhomogeneous linear equations

$$\sum_{n'_x n'_y n'_z} \mathcal{M}^{(m)}_{n_x n_y n_z, n'_x n'_y n'_z} \phi^{(m)}_{n'_x n'_y n'_z} = S^{(m)}_{n_x n_y n_z}, \tag{35}$$

with the matrix elements

$$\begin{aligned} &\mathcal{M}^{(m)}_{n_x n_y n_z, n'_x n'_y n'_z} \\ &= -\frac{1}{b_x^2}\left[\sqrt{(n_x+1)n'_x}\,\delta_{n_x n'_x - 2} + \sqrt{n_x(n'_x+1)}\,\delta_{n_x n'_x + 2}\right] \\ &\quad \times \delta_{n_y n'_y}\delta_{n_z n'_z} - \frac{1}{b_y^2}\left[\sqrt{(n_y+1)n'_y}\,\delta_{n_y n'_y - 2} + \sqrt{n_y(n'_y+1)}\right. \\ &\quad \left. \times \delta_{n_y n'_y + 2}\right]\delta_{n_x n'_x}\delta_{n_z n'_z} - \frac{1}{b_z^2}\left[\sqrt{(n_z+1)n'_z}\,\delta_{n_z n'_z - 2}\right. \\ &\quad \left. + \sqrt{n_z(n'_z+)}\,\delta_{n_z n'_z + 2}\right]\delta_{n_x n'_x}\delta_{n_y n'_y} + \left[\frac{n_x + \frac{1}{2}}{b_x^2}\right. \\ &\quad \left. + \frac{n_y + \frac{1}{2}}{b_y^2} + \frac{n_z + \frac{1}{2}}{b_z^2} + m_m^2\right]\delta_{n_x n'_x}\delta_{n_y n'_y}\delta_{n_z n'_z}, \end{aligned} \tag{36}$$

and the inhomogeneous parts

$$\begin{aligned} S^{(\sigma)}_{n_x n_y n_z} &= -\int d^3\mathbf{r}\ \varphi_{n_x}(x)\varphi_{n_y}(y)\varphi_{n_z}(z)(g_\sigma \rho_s(\mathbf{r}) \\ &\quad + g_2\sigma^2(\mathbf{r}) + g_3\sigma^3(\mathbf{r})), \end{aligned} \tag{37}$$

$$\begin{aligned} S^{(\omega^\mu)}_{n_x n_y n_z} &= +\int d^3\mathbf{r}\ \varphi_{n_x}(x)\varphi_{n_y}(y)\varphi_{n_z}(z)(g_\omega j^\mu_v(\mathbf{r}) \\ &\quad - c_3\omega^\nu(\mathbf{r})\omega_\nu(\mathbf{r})\omega^\mu(\mathbf{r})), \end{aligned} \tag{38}$$

$$S^{(\rho^\mu)}_{n_x n_y n_z} = +\int d^3\mathbf{r}\varphi_{n_x}(x)\varphi_{n_y}(y)\varphi_{n_z}(z) g_\rho j_3^\mu(\mathbf{r}). \tag{39}$$

The densities and currents in the source terms are obtained from the nucleon wave functions in Eq. (7). For the evaluation of the Coulomb field, due to its long-range character, an expansion in oscillator states is very difficult; therefore we use the standard Green's function method of Ref. [86] for the calculation of the Coulomb field in each step of the iteration.

The expansion for the spinors and meson fields has to be truncated to a fixed number of basis states. The cutoff parameters of the expansion are taken as $n_x + n_y + n_z \leqslant N_f = 8$ for large components of the nucleon spinors and $n_x + n_y + n_z \leqslant N_b = 20$ for the meson fields. Of course, as discussed in Ref. [87], the small components of the nucleon spinors have to be expanded up to $n_x + n_y + n_z \leqslant N_f + 1$ to avoid spurious solutions of the Dirac equations. When we increase the configuration space for the Fermions from $N_f = 8$ to $N_f = 10$, we find changes of only up to 0.6% for the total energies and up to 4% for the total quadrupole moments for the ground state of the nucleus ^{142}Gd investigated in this work. For $N_f = 8$ and $N_f = 10$ the same structures for the single-particle levels are obtained. Therefore, $N_f = 8$ and $N_b = 20$ are adopted in the present calculations. The parameter set PK1 [88] has been used for the Lagrangian. In the present calculations, pairing correlations are not taken into account.

As we have seen in the Introduction, magnetic rotation occurs if specific proton and neutron configurations are adopted as, for instance, the configuration $\pi h_{11/2}^2 \otimes \nu h_{11/2}^{-2}$ in the nucleus ^{142}Gd. This means that at the bandhead (i.e., for $\Omega = |\boldsymbol{\Omega}| = 0$), the two proton particles have an oblate density

distribution and the two neutron holes have a prolate density distribution.

First we solve the coupled system of Dirac (4) and Klein-Gordon (6) equations for the ground state, i.e., for $\Omega = |\mathbf{\Omega}| = 0$, filling in each step of the iteration the proton and neutron levels according to their energy from the bottom of the well. We calculate the quadrupole moments of the density distribution as defined in Eq. (13) and derive from this information the relative length of the principal axis of this distribution $R_x = \sqrt{\langle x^2 \rangle}$, $R_y = \sqrt{\langle y^2 \rangle}$, and $R_z = \sqrt{\langle z^2 \rangle}$. This leads in general to a triaxial ground state deformation, and without loss of generality we choose the axis in such a way that the x axis is the shortest axis and the z axis is the longest axis, i.e.,

$$R_x < R_y < R_z. \tag{40}$$

We can always enforce this condition by choosing proper initial deformations for the iterative solution.

In the next step, we consider the band with the configuration $\pi h_{11/2}^2 \otimes \nu h_{11/2}^{-2}$ with maximally aligned proton-particle and neutron-hole pairs. We choose the orientation of these pairs in such a way that the resulting density distributions of the protons and neutrons have a maximal overlap with that of the core. To determine the wave function of such a configuration, we solve the cranked RMF equations iterating with fixed configurations; i.e., in each step of the iteration, we determine the densities and currents [Eq. (7)] by occupying two proton $h_{11/2}$ levels and keeping two neutron $h_{11/2}$ levels empty, filling only the rest of the levels according to their energy from the bottom of the well. Since the density distribution of the two proton particles is oblate, we obtain the maximal overlap with the core, thereby fulfilling the condition (40) by orienting the two protons along the shortest axis (x axis), i.e., by occupying the maximally aligned configurations $(\pi h_{11/2}, m_x = \frac{11}{2}; \pi h_{11/2}, m_x = \frac{9}{2})$. The density distribution of the two neutron holes is prolate, and therefore we obtain the maximal overlap with the core by orienting the two neutron holes along the longest axis (z axis), i.e., keeping the maximally aligned configurations $(\nu h_{11/2}, m_z = -\frac{11}{2}; \nu h_{11/2}, m_z = -\frac{9}{2})$ empty. In the following, we say in a shorthand notation that we *block* these configurations, which means we occupy the corresponding proton levels and keep the corresponding neutron levels empty. The remaining orbits in the intruder shell for the protons $(\pi h_{11/2})$ are kept empty, and the remaining orbits in the intruder shell for the neutrons $(\nu h_{11/2})$ are kept occupied.

The configurations to be blocked are usually given in the spherical basis, i.e., by the spherical quantum numbers $|nljm\rangle$. The equations of motion are solved by expanding the Dirac spinors in terms of the three-dimensional harmonic oscillator functions in the Cartesian basis [Eq. (31)] labeled by the quantum number $|n_x, n_y, n_z, \pm i\rangle$. The resulting single-particle wave functions are often distributed over many components in the Cartesian basis, and it is not easy to identify the orbits which have to be blocked. To identify these orbits, we therefore transform the wave functions from the Cartesian basis with the quantum number $|n_x n_y n_z \pm i\rangle$ to a spherical basis with the quantum numbers $|nljm\rangle$ using the techniques given in Refs. [89,90] and block those levels, which have the maximal overlap with the required $|nljm\rangle$ configurations. These techniques are considerably simplified if we work in an isotropic Cartesian basis with identical basis parameters $b_x = b_y = b_z = b$ in Eq. (22). Since the deformations are small in bands with magnetic rotation, we use in the following calculations an isotropic Cartesian basis with $\hbar\omega_0 = 41A^{-1/3}$ and with the deformation parameters $\beta_0 = \gamma_0 = 0$.

Because of the considerable K mixing in TAC solutions and because of the high level density in such three-dimensional calculations, it occurs that the character of the blocked configurations is changing during the iteration. This means that we have to check in each step of the iteration the character of the blocked configurations. In particular, we have to determine the maximal component of the blocked configuration in the spherical basis sets $|nljm_x\rangle$ (for protons) and $|nljm_z\rangle$ (for neutrons). If this configuration no longer corresponds to the specific configuration we are interested in, we have to change the blocked configuration.

In details the situation is often even more complicated. Of course, the quantum number m depends on the quantization axis of this spherical basis. For $\Omega = 0$, where the core has its principal axes in the x, y, and z directions, the two proton particles in the $\pi h_{11/2}$ orbit fully aligned to the x axis correspond to $m_x = \frac{11}{2}$ and $m_x = \frac{9}{2}$, and the two neutron holes in the $\nu h_{11/2}$ orbit fully aligned to the z axis correspond to $m_z = -\frac{11}{2}$ and $m_z = -\frac{9}{2}$. Because of the rotational invariance around the y axis of the entire system, it can occur that the nucleus assumes a different orientation during the iteration. In this case, we have to first determine this orientation by calculating the quadrupole tensor $Q_{2\mu}$. Then we have to determine the wave functions in the spherical basis quantized along this new x axis for the proton particles and the new z axis for the neutron holes. Of course, if the quadratic constraint in Eq. (16) is strictly fulfilled, we do not need this additional rotation of the basis in the xz plane. However, this is not always the case during the iteration. As an example we show in Fig. 1, for the angular velocity $\hbar\Omega = 0.1$ MeV with the

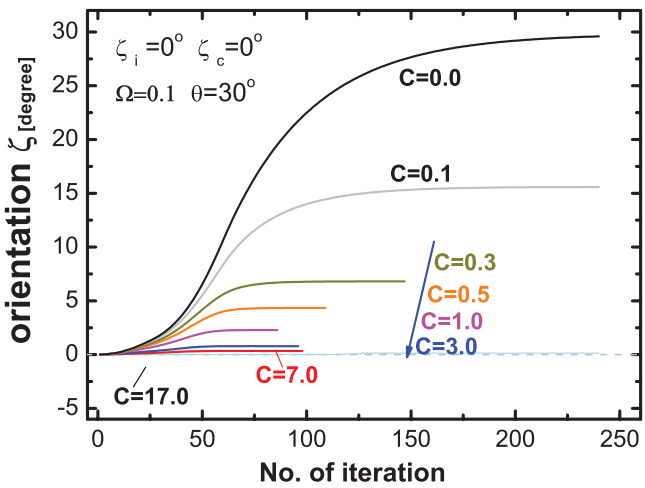

FIG. 1. (Color online) Angle ζ between the longest principal axis of the density distribution and the z axis as a function of the number of iterations for various values of the spring constant C of the quadratic constraint in Eq. (17). In each case, the iteration is started with $\zeta = 0$.

orientation angle $\theta_\Omega = 30^\circ$, the resulting angle ζ between the longest axis of the nucleus and the z axis as a function of the number of iterations and for various values of the spring constant C defined in Eq. (17). In each case we start with $\zeta = 0$. For small values of C the iteration converges to a finite angle ζ. Only for relatively large C values can the longest axis of the density distribution be kept parallel to the z axis ($\zeta = 0$).

So far we have discussed the situation for $\Omega = |\boldsymbol{\Omega}| = 0$. Going to finite values of Ω, we first choose a certain orientation $\theta_{\boldsymbol{\Omega}}$ of $\Omega = (\Omega \sin\theta_\Omega, 0, \Omega\cos\theta_\Omega)$, which is then kept fixed. We proceed in small steps of $\Omega = 0 \to \Omega_1 = \delta\Omega, \ldots, \Omega = \Omega_n \to \Omega_{n+1} = \Omega_n + \delta\Omega$. Of course, for finite values of Ω, the blocking criterion $(\pi h_{11/2}, m_z = \frac{11}{2}; \pi h_{11/2}, m_z = \frac{9}{2})$ for the protons and $(\nu h_{11/2}, m_x = \frac{11}{2}; \nu h_{11/2}, m_x = \frac{9}{2})$ for the neutrons can no longer be strictly applied, because we have to allow that the shears mechanism aligns the proton and neutron configurations more and more to the rotational axis with increasing values of Ω. For the solution for $\Omega = \Omega_{n+1}$ we therefore first determine the blocking structure of the solution obtained for $\Omega = \Omega_n$, i.e., counting the levels from the bottom of the well, we determine the numbers of the blocked levels. In each of the following iterations, we use the same blocking structure, i.e., we block the levels with the same numbers. It can occur that the configuration is changing when we go from $\Omega_n \to \Omega_n + \delta\Omega$, and in this case we have to reoccupy some levels, i.e., to change the blocking structure. We adopt the following prescription: starting from the Dirac level $|\psi_i(\Omega_n)\rangle$ blocked for $\Omega = \Omega_n$, we block for $\Omega = \Omega_{n+1}$ the orbit j which maximizes the overlap $\langle\psi_i(\Omega_n)|\psi_j(\Omega_{n+1})\rangle$, i.e.,

$$\langle\psi_j(\Omega + \delta\Omega)|\psi_i(\Omega)\rangle = 1 + \mathcal{O}(\delta\Omega). \tag{41}$$

This means, in particular, that we have to store the single-particle Dirac spinors of the solution for $\Omega = \Omega_n$ during the calculation for $\Omega = \Omega_{n+1}$. For infinitesimal step sizes, this condition corresponds to the concept of parallel transport [91,92]. In the case of an avoided level crossing, this condition requires that infinitesimal step sizes stay in an adiabatic way on the lower (or upper) level. After many infinitesimally small adiabatic steps, this would lead to a change in the configuration during the level crossing. For finite step sizes $\delta\Omega$, this condition corresponds to a diabatic crossing and avoids in this case the change of configuration. We therefore use in the following calculations the finite step size $\hbar\delta\Omega = 0.05$ MeV.

In summary, we start for each orientation angle θ_Ω at $\Omega = 0$, determine here the blocking configuration for the protons and neutrons by occupying or keeping empty the levels with maximal alignment in the $1h_{11/2}$ intruder shells. Afterward, for fixed orientation angle θ_Ω, we increase Ω successively in steps of $\hbar\delta\Omega = 0.05$ MeV and apply in each case the prescription (41) for the occupation of the various intruder levels.

IV. RESULTS AND DISCUSSION

Bands with magnetic rotation have been observed in the mass regions $A \sim 80, 100, 130$, and 200. For ^{142}Gd, five bands, denoted as DB1, DB2, DB3, DB4, and DB5, have been observed experimentally, and four of them have been interpreted as magnetic rotation bands with the configurations $\pi h^2_{11/2} \otimes \nu h^{-2}_{11/2}$, $\pi h^2_{11/2} \otimes \nu h^{-4}_{11/2}$, $\pi h^1_{11/2} \otimes \pi g^{-1}_{7/2} \nu h^{-2}_{11/2}$, and $\pi h^1_{11/2} \otimes \pi g^{-1}_{7/2} \nu h^{-4}_{11/2}$ [93,94], respectively. Using the nonrelativistic Skyrme-Hartree-Fock method with tilted axis cranking, the shears mechanism and the spectrum of the band DB1 in ^{142}Gd have been investigated in Refs. [38,95]. In the present paper, we apply the relativistic TAC approach to describe the same band DB1 and investigate the characteristic of magnetic rotation in a relativistic microscopic and self-consistent theory.

In TAC calculations, the tilted angle θ_Ω of the orientation of the angular velocity $\boldsymbol{\Omega}$ with respect to the principal axis of the density distribution should be determined in a self-consistent way. Such a self-consistent procedure turns out to be very time consuming. In the literature, so far, this has not been done; therefore we also start our calculations with the reasonable approximation to freeze the tilted angle for all Ω values at the value for $\Omega = 0$, i.e., at $\theta_\Omega = 45^\circ$. Afterward, we will carry out a self-consistent determination of the rotational angle. As we will see, this will improve the agreement with experimental data.

A. Frozen orientation of the angular velocity Ω at $\theta_\Omega = 45^\circ$

In this investigation, we consider the configuration $\pi h^2_{11/2} \otimes \nu h^{-2}_{11/2}$ for the band DB1 in the nucleus ^{142}Gd and solve the relativistic TAC equations for this configuration with the parameter set PK1 [88] in a self-consistent way. For $\Omega = 0$, the two protons in the $\pi h_{11/2}$ orbit contribute roughly $10\hbar$ of angular momentum parallel to the short axis (x axis), and the two neutron holes in the $\nu h_{11/2}$ orbit contribute roughly $10\hbar$ angular momentum along the long axis (z axis). Therefore the total angular momentum arising in this configuration points in the direction $\theta_J = 45^\circ$, i.e., one has a tilted angle $\theta_\Omega := \sphericalangle(\boldsymbol{\Omega}, \mathbf{e}_x) = 45^\circ$, and it is a reasonable approximation to freeze the value of the tilted angle at the value $\theta_\Omega = 45^\circ$ for all higher Ω values. With this approximation, we solve these equations for various rotational frequencies, starting at $\hbar\Omega = 0.0$ MeV and increasing in steps of 0.05 MeV going up to $\hbar\Omega = 0.55$ MeV. As discussed in the last section for $\Omega = 0$, the proton orbits $(\pi h_{11/2}, m_x = \frac{11}{2}; \pi h_{11/2}, m_x = \frac{9}{2})$ are occupied and the neutron orbits $(\nu h_{11/2}, m_z = -\frac{11}{2}; \nu h_{11/2}, m_z = -\frac{9}{2})$ are kept empty. Starting with this solution, we use the prescription (41) for the occupation with increasing Ω values.

In Table I, we show the deformation parameters β and γ of the self-consistent density distribution found in these TAC calculations with frozen orientation of the angular velocity $\theta_\Omega = 45^\circ$ as a function of the rotational frequency Ω. The deformation parameter β decreases slowly, except for a small fluctuation around $\hbar\Omega = 0.40$ MeV, from $\beta = 0.148$ at $\hbar\Omega = 0.00$ MeV down to $\beta = 0.142$ at $\hbar\Omega = 0.55$ MeV, and the deformation γ changes from $\gamma = -46.6^\circ$ at $\hbar\Omega = 0.00$ MeV to $\gamma = -38.5^\circ$ at $\hbar\Omega = 0.55$ MeV.

In Fig. 2, the energies of the band DB1 in the nucleus ^{142}Gd, which starts with the configuration $\pi h^2_{11/2} \otimes \nu h^{-2}_{11/2}$, are shown as a function of the angular momentum I determined by the cranking condition in Eq. (11). The results of TAC RMF calculations are shown by open squares and compared with experimental data (filled circles) of the band DB1 in Ref. [94] and with nonrelativistic Skyrme-Hartree-Fock (SHF)

TABLE I. Deformation parameters of the $\pi h_{11/2}^2 \otimes \nu h_{11/2}^{-2}$ band in the nucleus ^{142}Gd as functions of the rotational frequency Ω (in MeV). The results are obtained from tilted axis cranking RMF calculations with the parameter set PK1 and with frozen orientation ($\theta_\Omega = 45^\circ$) of the cranking axis.

Ω	0.00	0.10	0.15	0.20	0.25	0.30	0.35	0.40	0.45	0.50	0.55
β	0.148	0.148	0.148	0.147	0.147	0.146	0.145	0.145	0.145	0.147	0.142
γ	-46.6°	-44.6°	-43.9°	-43.4°	-43.1°	-42.7°	-42.6°	-42.4°	-42.3°	-40.1°	-38.5°

calculations of Ref. [38] (open triangles). As no link to the ground state is observed, we adopt the recommended band head spin $I = 16\hbar$ of Ref. [94], and we take the energy at $I = 16\hbar$ as a reference for both the RMF values and the nonrelativistic SHF calculations. Compared with the nonrelativistic SHF results, the experimental energies are well reproduced in the relativistic TAC calculations with the frozen orientation $\theta_\Omega = 45^\circ$. This is a strong indication that bands based on magnetic rotation can be well understood in the framework of relativistic tilted axis cranking even with the approximation of a frozen orientation angle. The calculated values for angular momenta $I = 20\hbar$ and $I = 21\hbar$ are missing in Fig. 2, because, working with constant Ω, at these values we could not find converged solutions. In fact, as we will see in the next section, we observe a level crossing in this region. One proton level from the $1g_{7/2}$ shell crosses with a proton level from the $2d_{5/2}$ shell. Since it is well known that level crossings cannot be described properly by the cranking formalism [96], we omitted the energy values for $I = 20\hbar$ and $I = 21\hbar$. As we will see in the next section, the values for $I \geqslant 22\hbar$ obtained by the prescription (41) belong more or less to the configuration $\pi[h_{11/2}^2 g_{7/2}^{-1} d_{5/2}^1] \otimes \nu h_{11/2}^{-2}$, and the value for $I = 22\hbar$ is in agreement with experiment.

Next we show in Fig. 3 the angular momentum I defined in Eq. (11) for this band. The relativistic TAC calculations with frozen orientation of the tilted axis are shown by open squares as a function of the rotational frequency. They are compared with the experimental values (filled circles) of Ref. [94], where the experimental rotational frequency has been calculated by means of the condition [34]

$$\hbar\Omega_{\rm exp} = \frac{1}{2}[E_\gamma(I+1 \to I) + E_\gamma(I \to I-1)] \approx \frac{dE}{dI}. \tag{42}$$

Both the calculated and the experimental angular momenta $I(\Omega)$ agree with each other and form nearly straight lines up to $\hbar\Omega = 0.4$ MeV. However, at $\hbar\Omega = 0.4$ MeV, a backbending is observed in the experimental band, which corresponds to the level crossing discussed above. It is obviously not described in our calculations, where we observe no solution for $I = 20\hbar$ and $I = 21\hbar$. It is a well-known deficiency of cranking calculations [96] that sharp backbending phenomena are usually smeared out in this semiclassical approximation because of the spurious mixing induced by the variation at fixed angular velocity instead of fixed angular momentum.

To examine the shears mechanism for the band DB1 in the nucleus ^{142}Gd, we show in Fig. 4 the proton and neutron angular momentum vectors $\mathbf{J}_\pi$ and $\mathbf{J}_\nu$ defined as

$$\mathbf{J}_\pi = \langle\hat{\mathbf{J}}_\pi\rangle = \sum_{p=1}^{Z}\langle p|\hat{j}|p\rangle, \quad \mathbf{J}_\nu = \langle\hat{\mathbf{J}}_\nu\rangle = \sum_{n=1}^{N}\langle n|\hat{j}|n\rangle, \tag{43}$$

where the sum runs over all the proton (or neutron) levels occupied in the cranking wave function in the intrinsic system. The abscissa corresponds to the short axis (x axis) and the ordinate corresponds to the long axis (z axis). The different panels in this figure correspond to results of relativistic TAC calculations for various angular velocities Ω. Again we used

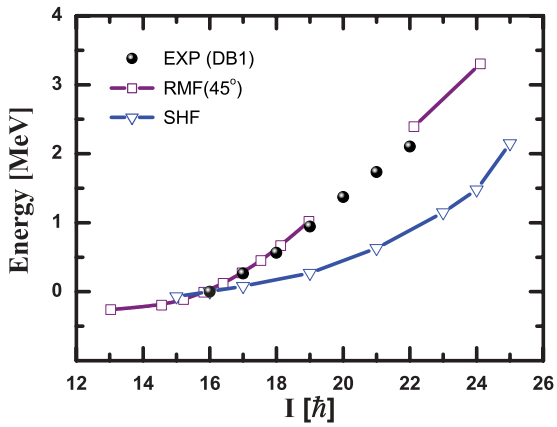

FIG. 2. (Color online) Energy in the tilted axis cranking RMF calculation with frozen orientation $\theta_\Omega = 45^\circ$ and the configuration $\pi h_{11/2}^2 \otimes \nu h_{11/2}^{-2}$ at the bandhead as a function of the total angular momentum for band DB1 in ^{142}Gd compared with the data [94] and nonrelativistic SHF results [38].

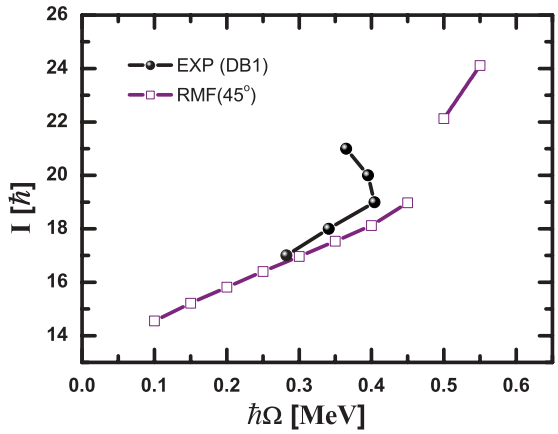

FIG. 3. (Color online) Total angular momentum in the tilted axis cranking RMF calculation with frozen orientation $\theta_\Omega = 45^\circ$ and the configuration $\pi h_{11/2}^2 \otimes \nu h_{11/2}^{-2}$ at the bandhead as a function of the rotational frequency for band DB1 in ^{142}Gd compared with the data [94].

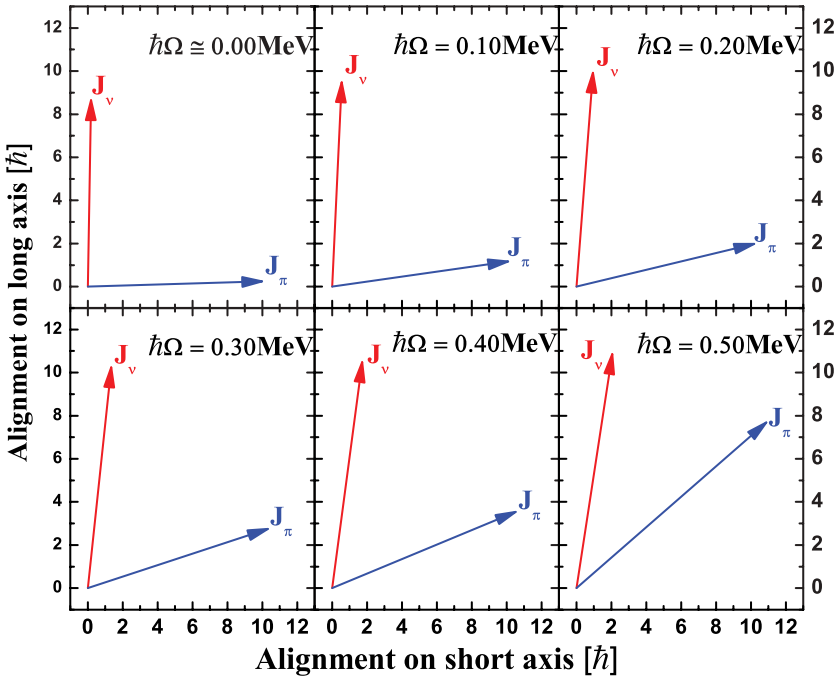

FIG. 4. (Color online) Proton and neutron angular momentum $\mathbf{J}_\pi$ and $\mathbf{J}_\nu$ in tilted axis cranking RMF for frozen orientation $\theta_\Omega = 45^\circ$ and the configuration $\pi h_{11/2}^2 \otimes \nu h_{11/2}^{-2}$ at the bandhead in the plane spanned by the shortest and longest axes of the nucleus for several rotational frequencies Ω.

the parameter set PK1 and a frozen orientation angle $\theta_\Omega = 45^\circ$ starting with the fixed aligned configuration $\pi h_{11/2}^2 \otimes \nu h_{11/2}^{-2}$ and using the condition (41) with increasing angular velocity.

For band DB1 in the nucleus ^{142}Gd with the configuration $\pi h_{11/2}^2 \otimes \nu h_{11/2}^{-2}$, the contributions to the angular momentum come mainly from the two proton particles and the two neutron holes. At the band head, two protons filling the bottom of the $h_{11/2}$ shell contribute around $10\hbar$ of angular momentum along the short axis, and the two neutron holes at the upper end of the $h_{11/2}$ shell contribute around $10\hbar$ angular momentum along the long axis. They form the two blades of the shears. After the rotation is switched on, the two blades move toward each other, closing the shears more and more. In such a way, the shears mechanism for the band DB1 in ^{142}Gd is clearly observed in Fig. 4.

To display the shears mechanism more explicitly, we show in Fig. 5 the shears angles Θ_π, Θ_ν, and Θ as defined in Ref. [37],

$$\cos\Theta_\pi = \frac{\mathbf{J}_\pi \mathbf{J}}{|\mathbf{J}_\pi||\mathbf{J}|}, \quad \cos\Theta_\nu = \frac{\mathbf{J}_\nu \mathbf{J}}{|\mathbf{J}_\nu||\mathbf{J}|}, \quad \Theta = \Theta_\pi + \Theta_\nu, \tag{44}$$

extracted from the results of our relativistic TAC calculation as a function of the rotational frequency Ω for band BD1 in ^{142}Gd. The shears angles Θ_π, Θ_ν, and Θ are, respectively, the angles between $\mathbf{J}_\pi$ and $\mathbf{J}$, $\mathbf{J}_\nu$ and $\mathbf{J}$, and $\mathbf{J}_\pi$ and $\mathbf{J}_\nu$. All of them decrease with the rotational frequency, i.e., the angular momenta of proton and neutron align toward each other with the increasing values of the cranking frequency Ω. This fact further confirms the picture of the shears mechanism. We note that the shears angles decrease almost linearly with the rotational frequency till $\hbar\Omega = 0.40$ MeV. After $\hbar\Omega = 0.45$ MeV, a different trend appears, and the reason for this sudden change is again the level crossing discussed below.

Of course, the present calculations do not represent fully self-consistent solutions of the TAC model, because, so far, we keep the orientation of the angular velocity fixed and at the same time we require by the quadratic constraint in Eq. (17) that the orientation of the density distribution is parallel to the x, y, and z axes. Therefore the orientation of the angular velocity given by the angle θ_Ω is no longer strictly parallel to the orientation of the angular momentum given by the angle θ_J in Eq. (12). However, as can be seen from Fig. 4, for $\hbar\Omega \leqslant 0.4$ MeV, the difference between θ_J and θ_Ω is negligible. This shows that in this region the approximation of a frozen orientation of $\mathbf{\Omega}$ is a reasonable approximation. We also recognize in Fig. 4 that for $\hbar\Omega > 0.4$ MeV, this approximation is no longer valid. This will be discussed in more detail in the next section.

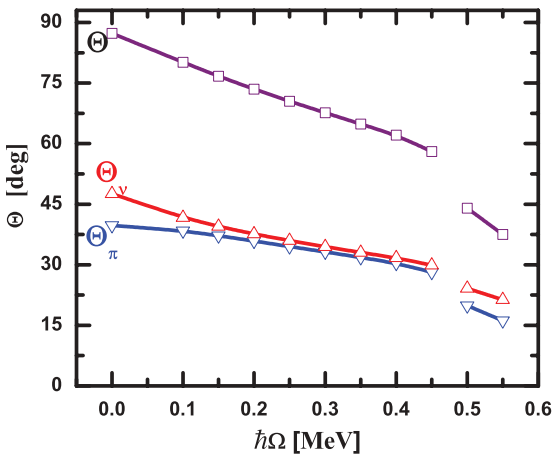

FIG. 5. (Color online) Shears angles Θ_π, Θ_ν, and Θ in a tilted axis cranking RMF calculation with frozen $\theta_\Omega = 45^\circ$ and the configuration $\pi h_{11/2}^2 \otimes \nu h_{11/2}^{-2}$ at the bandhead as functions of the rotational frequency for band BD1 in ^{142}Gd.

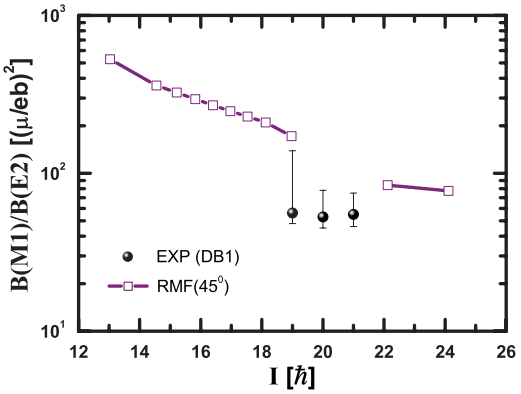

FIG. 6. (Color online) Ratio $B(M1)/B(E2)$ as a function of the total angular momentum for band BD1 in a tilted axis cranking RMF calculation with frozen orientation $\theta_\Omega = 45^\circ$ and the configuration $\pi h_{11/2}^2 \otimes \nu h_{11/2}^{-2}$ at the bandhead compared with the data.

A typical characteristic of magnetic rotation is strongly enhanced $B(M1)$ transitions at low angular momenta as well their decrease with the angular momentum. Therefore, we give in Table II the $B(M1)$ and $B(E2)$ values and compare them with the experimental data of Refs. [93,94]. Here the $B(M1)$ values are derived from the relativistic form of the effective current operator in Eq. (18). We find that the calculated $B(E2)$ values are below 0.03 $(e\ \mathrm{b})^2$, and the $B(M1)$ values are about in the range of 1–3 $(\mu_N)^2$. In Fig. 6, we show the ratio $B(M1)/B(E2)$ between magnetic and electric transitions as a function of the total angular momentum for the band BD1 in the nucleus ^{142}Gd calculated in the tilted axis cranking RMF with the configuration $\pi h_{11/2}^2 \otimes \nu h_{11/2}^{-2}$ and compare this ratio with data. The calculated $B(M1)/B(E2)$ values decrease with rotational frequency and exhibit the typical property of magnetic rotation. Since the electromagnetic transition data are available only in the range of the backbending phenomenon [94], future experiments in the lower spin region are welcome.

TABLE II. Angular momenta I (in $\hbar$), the $B(M1)$ values (in $\mu_N{}^2$) and $B(E2)$ values (in e^2 b^2) compared with the experimental values of Refs. [93,94]. The theoretical values I_{cal} are defined in Eq. (11).

I_{cal}	$B(M1)_{\mathrm{cal}}$	$B(E2)_{\mathrm{cal}}$	I_{exp}	$B(M1)_{\mathrm{exp}}$	$B(E2)_{\mathrm{exp}}$
13.03	3.415	0.65×10^{-2}	–	–	–
14.55	3.304	0.92×10^{-2}	–	–	–
15.21	3.177	0.98×10^{-2}	–	–	–
15.81	3.039	1.03×10^{-2}	–	–	–
16.40	2.899	1.08×10^{-2}	–	–	–
16.97	2.762	1.11×10^{-2}	–	–	–
17.53	2.628	1.15×10^{-2}	–	–	–
18.12	2.494	1.19×10^{-2}	–	–	–
18.97	2.310	1.34×10^{-2}	19	$1.29^{+0.95}_{-0.25}$	$1.7^{+1.9}_{-0.7} \times 10^{-2}$
–	–	–	20	$1.10^{+0.77}_{-0.20}$	$1.8^{+1.6}_{-0.5} \times 10^{-2}$
–	–	–	21	$1.04^{+0.38}_{-0.18}$	$1.7^{+0.9}_{-0.4} \times 10^{-2}$
22.12	1.783	2.12×10^{-2}	–	–	–
24.10	1.517	1.96×10^{-2}	–	–	–

In the previous calculation for ^{84}Rb [37], an attenuation factor around 0.3 was introduced to improve the agreement with experimental $B(M1)/B(E2)$ ratios. This factor took care of the fact that the nonrelativistic form of the magnetic moment operator had been used in Ref. [37]. The $B(M1)$ value at $I = 19$ calculated from Eq. (18) is $2.31\mu_N{}^2$, around one-third of the value $7.29\mu_N{}^2$ obtained in Ref. [37] from the nonrelativistic definition.

B. Self-consistent RMF shears results

In TAC calculations, the orientation θ_Ω of the angular velocity $\boldsymbol{\Omega}$ with respect to the principal axis of the density distribution should be determined in a self-consistent way either by minimizing the total Routhian

$$E'(\Omega, \theta_\Omega) = \langle \hat{H} - \cos\theta_\Omega \Omega \hat{J}_x - \sin\theta_\Omega \Omega \hat{J}_z \rangle, \qquad (45)$$

for fixed values of Ω with respect to θ_Ω or by requiring that $\boldsymbol{\Omega}$ is parallel with $\mathbf{J}$ at fixed Ω. The tilted angle corresponding to the minimum at fixed Ω is the so-called self-consistent rotational angle. Such a self-consistent procedure is in principle necessary but turns out to be very time consuming.

As in the nonrelativistic calculations of Ref. [38], all the TAC calculations discussed so far have been carried out by freezing the tilted angle for all Ω values at $\theta_\Omega = 45^\circ$, its value at $\Omega = 0$. As we have seen in the last section, this approximation was rather successful below $\hbar\Omega \leqslant 0.4$ MeV. The data available for the band DB1 in ^{142}Gd have been rather well reproduced, in particular, the spectra, electromagnetic transition $B(M1)/B(E2)$ ratios, relation between rotational frequency and angular momentum, and characteristic shears mechanism of magnetic rotation. Encouraged by the success of the approximation with a frozen tilted angle, we carried out tilted axis calculations in which the orientation of the angular velocity is determined in a self-consistent way; i.e., we repeat the earlier calculations with fixed orientation for various values of the angle θ_Ω starting at $\theta_\Omega = 0$ and increasing it in steps of 5°. For each θ_Ω value, we start at $\Omega = 0$ with the aligned configuration $\pi h_{11/2}^2 \otimes \nu h_{11/2}^{-2}$, and using the prescription given in Eq. (41), we determine the occupation for increasing Ω values as in the last section.

In Fig. 7, we plot the total Routhians (solid lines) as functions of the tilted angle θ_Ω for the various rotational frequencies Ω. According to the prescription of the cranking model, the minimum of the total Routhians with respect to θ_Ω for fixed value of Ω determines the *self-consistent rotational angle* θ_{self}. In Fig. 7, this angle is represented by full red dots. The dashed vertical line labels the Routhians corresponding to the calculations described in the last section with a frozen angle $\theta_\Omega = 45^\circ$.

As seen in Fig. 7 for rotational frequencies $\hbar\Omega \leqslant 0.40$ MeV, the main component for the minimum of the total Routhian corresponds to the configuration $\pi h_{11/2}^2 \otimes \nu h_{11/2}^{-2}$. Beyond $\hbar\Omega = 0.40$ MeV, the other competitor minimum appears corresponding to the configuration $\pi[h_{11/2}^2 g_{7/2}^{-1} d_{5/2}^1] \otimes \nu h_{11/2}^{-2}$, which is represented by green triangles in Fig. 7. It is clearly seen from this figure that the frozen $\theta_\Omega = 45^\circ$ is a good approximation of the self-consistent minimum in the Routhian

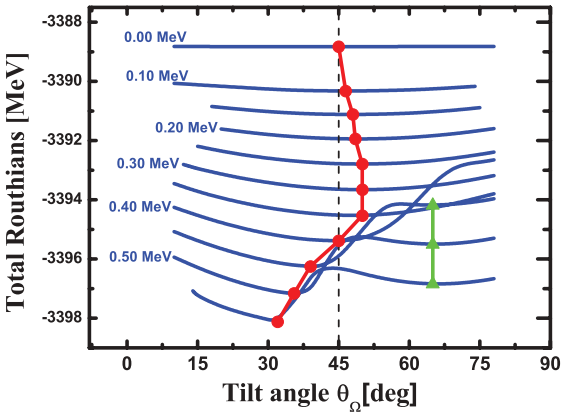

FIG. 7. (Color online) Total Routhians as functions of tilted angle θ_Ω for several rotational frequencies Ω in a self-consistent tilted axis cranking RMF calculation. The solid dots and triangles correspond to the configurations $\pi h_{11/2}^2 \otimes \nu h_{11/2}^{-2}$, and $\pi[h_{11/2}^2 g_{7/2}^{-1} d_{5/2}^1] \otimes \nu h_{11/2}^{-2}$, respectively.

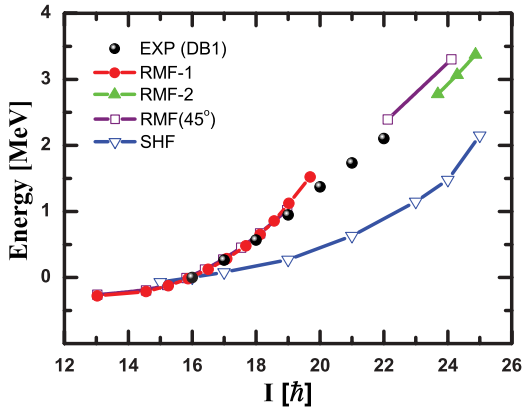

FIG. 9. (Color online) Energy as a function of the total angular momentum in a tilted axis cranking RMF calculation for RMF-1 and RMF-2 compared with the data for band DB1 in ^{142}Gd [94]. The nonrelativistic SHF result [38] and the energy with frozen $\theta_\Omega = 45^\circ$ for the configuration $\pi h_{11/2}^2 \otimes \nu h_{11/2}^{-2}$ are also included.

curve for $\hbar\Omega \leqslant 0.40$ MeV, which explains why the magnetic rotation for DB1 in ^{142}Gd can be understood well by the tilted axis cranking RMF calculation with the frozen tilted angle.

For fixed Ω values, increasing the orientation angle θ_Ω results in a crossing between the proton levels $1g_{7/2}$ and $2d_{5/2}$. Because of this level crossing, in the calculation with frozen angle $\theta_\Omega = 45^\circ$ of the last section, the configuration $\pi h_{11/2}^2 \otimes \nu h_{11/2}^{-2}$ is no longer the dominant one but only the main component in the eigenfunction for $\hbar\Omega > 0.40$ MeV. Using the "parallel-transport" method, the level $1g_{7/2}$-1/2 after the level crossing should be occupied. However, such occupation will lead to a divergence. If the lower proton level $2d_{5/2}$ 1/2 instead of $1g_{7/2}$-1/2 is occupied, for $\hbar\Omega =$ 0.45, 0.50, and 0.55 MeV, other minima will appear in the Routhian curves, and they will correspond to the configuration $\pi[h_{11/2}^2 g_{7/2}^{-1} d_{5/2}^1] \otimes \nu h_{11/2}^{-2}$. That is, for the configuration $\pi h_{11/2}^2 \otimes \nu h_{11/2}^{-2}$, we could not get convergent results for $\hbar\Omega = 0.40$ MeV and $\theta_\Omega > 45^\circ$, as we did for $\hbar\Omega =$ 0.45 MeV and $\theta_\Omega > 39^\circ$, $\hbar\Omega = 0.50$ MeV and $\theta_\Omega > 36^\circ$, and $\hbar\Omega = 0.55$ MeV and $\theta_\Omega > 32^\circ$. Therefore the Routhians curve is not complete for $\hbar\Omega > 0.40$ MeV and configuration $\pi h_{11/2}^2 \otimes \nu h_{11/2}^{-2}$, and the corresponding minima marked in red dots with $\hbar\Omega > 0.40$ MeV in Fig. 7 may not be the real ones. As we will see in the following, the strong mixture of these configurations has an impact not only on the minima of the total Routhians, but also on the other physical observables of magnetic rotation. In the following, we consider the self-consistent solutions for the two minima as a function of Ω. They correspond to the configurations $\pi h_{11/2}^2 \otimes \nu h_{11/2}^{-2}$ and $\pi[h_{11/2}^2 g_{7/2}^{-1} d_{5/2}^1] \otimes \nu h_{11/2}^{-2}$ and will be referred to as

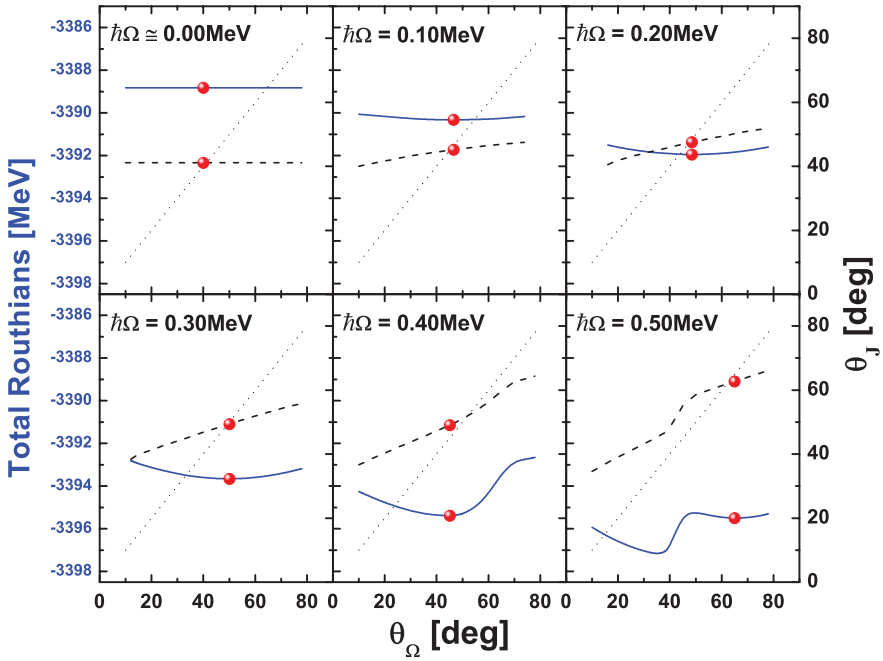

FIG. 8. (Color online) Total Routhians (solid blue line, left scale) and the orientation of the angular momentum θ_J (dashed black line, right scale) for various rotational frequencies Ω. The solid red dots correspond to the self-consistent angle $\theta_{\rm self}$ on both curves. For convenience, we also show the dotted line defined by $\theta_J = \theta_\Omega$.

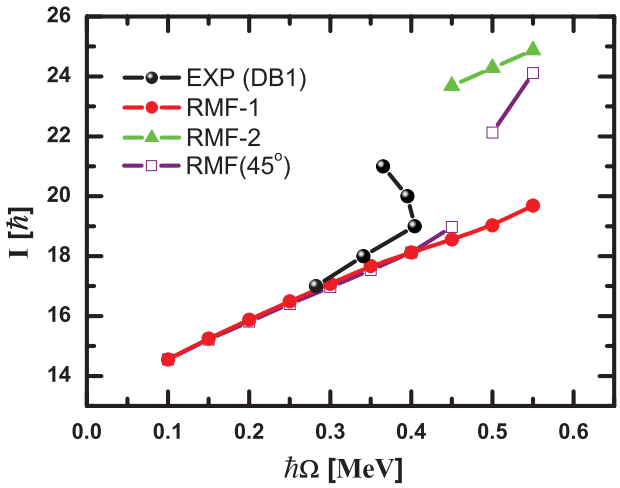

FIG. 10. (Color online) Total angular momentum as a function of the rotational frequency in tilted axis cranking RMF calculation with PK1 for the configurations $\pi h_{11/2}^2 \otimes \nu h_{11/2}^{-2}$ (RMF-1) and $\pi[h_{11/2}^2 g_{7/2}^{-1} d_{5/2}^1] \otimes \nu h_{11/2}^{-2}$ (RMF-2) compared with the data for DB1 in ^{142}Gd [94] and the results with PK1 and frozen $\theta_\Omega = 45^\circ$ for the configuration $\pi h_{11/2}^2 \otimes \nu h_{11/2}^{-2}$.

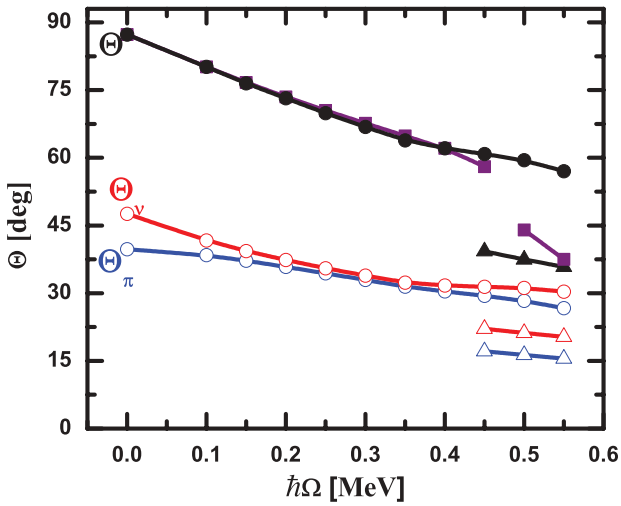

FIG. 11. (Color online) Shears angles Θ_π, Θ_ν (empty symbols) and $\Theta = \Theta_\pi + \Theta_\nu$ (solid symbols) in a tilted axis cranking RMF calculation for the RMF-1 (circles) and RMF-2 (triangles) configurations. For comparison, we also show the results for the total angle Θ for frozen orientation $\theta_\Omega = 45^\circ$ (squares) as discussed in Fig. 5.

RMF-1 and RMF-2, respectively. For the calculation of the configuration $h_{11/2}^2 \otimes h_{11/2}^{-2}$ with the frequencies $\hbar\Omega = 0.40$, 0.45, and 0.55 MeV, we used the values 45°, 39°, 36°, and 32° for the corresponding orientations of the angular velocity. These values correspond to local minima in the Routhian curves for $\hbar\Omega = 0.40, 0.45, 0.50$, and 0.55 MeV before the change of configuration.

In Fig. 8, we show for various Ω values the Routhian and the orientation of the angular momentum θ_J defined in Eq. (12) as functions of the orientation θ_Ω of the angular velocity $\boldsymbol{\Omega}$. The self-consistent angle (the minimum of the Routhian) is indicated by a solid dot on both curves. To clarify the situation, we also show the line $\theta_J = \theta_\Omega$. As it is clearly seen, for $\hbar\Omega < 0.40$ MeV the orientation of the angular velocity θ_Ω is nearly identical to the orientation of the angular momentum θ_J as expected for a self-consistent solution of the TAC problem. We also see that for $\hbar\Omega = 0.40$ MeV, self-consistency is not fully achieved, and for $\hbar\Omega > 0.40$ MeV, self-consistency is only achieved for the second minimum with the configuration $\pi[h_{11/2}^2 g_{7/2}^{-1} d_{5/2}^1] \otimes \nu h_{11/2}^{-2}$. In this region, the configuration $\pi h_{11/2}^2 \otimes \nu h_{11/2}^{-2}$ is an excited configuration, which is very hard to describe in cranking calculations. In Ref. [97], the cranking model was used to describe excited configurations by including an additional constraint of orthogonality. This has not been done in the present investigation, and therefore the solutions RMF-1 with the configuration $\pi h_{11/2}^2 \otimes \nu h_{11/2}^{-2}$ have to be considered only as approximate solutions for $\hbar\Omega >$ 0.40 MeV.

In Fig. 9, we show the energies as functions of the total angular momentum for the RMF-1 and RMF-2 calculations for band DB1 in ^{142}Gd. They are compared with the available data [94], the results of a frozen tilted angle $\theta_\Omega = 45^\circ$, and the nonrelativistic SHF results [38]. As in Fig. 2, the energy at $I = 16\,\hbar$ is taken as a reference. In general, the energies in the RMF calculations achieve better agreement with the data than do the SHF results. The energies in the RMF calculation with frozen $\theta_\Omega = 45^\circ$ coincide with the results of RMF-1 at low spin and are close to the results of RMF-2 at high spin.

The deformation parameters β and γ in the tilted axis cranking RMF with the configuration $\pi h_{11/2}^2 \otimes \nu h_{11/2}^{-2}$ are given in Table III. For increasing rotational frequencies Ω, the deformation β smoothly decreases from 0.149 for $\Omega = 0$ to 0.139 for $\hbar\Omega = 0.55$ MeV, and the deformation γ changes from -46.6° for $\Omega = 0$ to -41.9° for $\hbar\Omega = 0.55$ MeV.

In Fig. 10, the total angular momenta are shown as functions of the rotational frequency and results of RMF-1 and RMF-2 calculations are compared with data of Ref. [94] and with the results of frozen angle $\theta_\Omega = 45^\circ$.

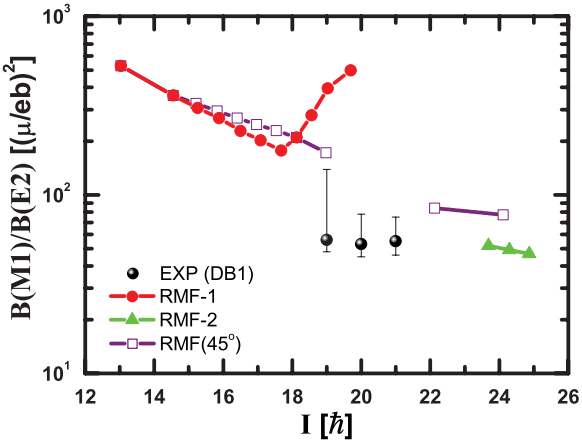

FIG. 12. (Color online) Ratios of $B(M1)/B(E2)$ as a function of the total angular momentum in tilted axis cranking RMF calculation with PK1 for the configurations $\pi h_{11/2}^2 \otimes \nu h_{11/2}^{-2}$ (RMF-1) and $\pi[h_{11/2}^2 g_{7/2}^{-1} d_{5/2}^1] \otimes \nu h_{11/2}^{-2}$ (RMF-2) compared with the data for DB1 in ^{142}Gd [94] and the results with PK1 and frozen $\theta_\Omega = 45^\circ$ for the configuration $\pi h_{11/2}^2 \otimes \nu h_{11/2}^{-2}$.

TABLE III. Deformation parameters as in Table I, but for the self-consistent value of θ_Ω at each angular velocity Ω.

Ω	0.00	0.10	0.15	0.20	0.25	0.30	0.35	0.40	0.45	0.50	0.55
β	0.148	0.148	0.148	0.147	0.146	0.146	0.145	0.145	0.144	0.142	0.139
γ	-46.6°	-44.6°	-43.9°	-43.4°	-43.1°	-43.0°	-42.8°	-42.3°	-41.9°	-41.6°	-41.9°

The total angular momenta in RMF-1 linearly increase with the rotational frequency and agree with the data until $\hbar\Omega = 0.40$ MeV. After $\hbar\Omega > 0.40$ MeV, an upbending is observed for the data. This upbending cannot be reproduced by the smooth behavior in either RMF-1 or RMF-2 calculations. The curve $I(\Omega)$ with frozen $\theta_\Omega = 45^\circ$ links in some respect the results with those for the configurations $\pi h^2_{11/2} \otimes \nu h^{-2}_{11/2}$ and $\pi[h^2_{11/2} g^{-1}_{7/2} d^1_{5/2}] \otimes \nu h^{-2}_{11/2}$. This provides a qualitative explanation for the experimental upbending.

The shears angles Θ_π, Θ_ν, and Θ in RMF-1 and RMF-2 are shown in Fig. 11 in comparison with the results with frozen angle $\theta_\Omega = 45^\circ$. The shears angles in RMF-1 linearly decrease with Ω, which exhibits a pronounced shears mechanism, i.e., the proton and neutron angular momenta align toward each other with increasing rotational frequency Ω. Compared with the previous results of frozen $\theta_\Omega = 45^\circ$, the RMF-1 shears angles continue to decrease smoothly with Ω when $\hbar\Omega \geqslant 0.40$ MeV. The results with frozen angle $\theta_\Omega = 45^\circ$ decrease much faster for $\hbar\Omega \geqslant 0.40$ MeV and approach the results of RMF-2 for $\hbar\Omega = 0.55$ MeV.

Finally, the ratio $B(M1)/B(E2)$ in RMF-1 and RMF-2 are given in comparison with the data and results with frozen angle $\theta_\Omega = 45^\circ$ in Fig. 12. The ratio $B(M1)/B(E2)$ in RMF-1 decreases with the spin until $\hbar\Omega = 0.40$ MeV ($I = 18\hbar$) and increases again. The results in RMF-2 appear after $I = 23.7\hbar$. The data available happen to be located in the band crossing region. The calculated $B(E2)$ are below 0.03 $(e\,\mathrm{b})^2$, and the $B(M1)$ are in the range of 1–3 $(\mu_N)^2$. The ratios $B(M1)/B(E2)$ with frozen $\theta_\Omega = 45^\circ$ link the results in RMF-1 and RMF-2. Therefore it is easy to understand why it gives the best description for the ratio $B(M1)/B(E2)$. In Fig. 13, we show as in Fig. 8 the total Routhians and the $B(M1)/B(E2)$ values for various angular velocities Ω as functions of the orientation angle θ_Ω. We observe that for fixed and large absolute values of the rotational frequency Ω, the $B(M1)/B(E2)$ value depends strongly on the orientation angle θ_Ω. For $\hbar\Omega \geqslant 0.40$ MeV, the RMF-2 solution with the configuration $\pi[h^2_{11/2} g^{-1}_{7/2} d^1_{5/2}] \otimes \nu h^{-2}_{11/2}$ shows decreasing values for $B(M1)/B(E2)$. On the other hand, the orientation angles θ_Ω adopted in the calculation of $B(M1)$ and $B(E2)$ for $\hbar\Omega \geqslant 0.40$ MeV are not the virtual minima in the Routhians curves shown in Fig. 7 for the configuration $\pi h^2_{11/2} \otimes \nu h^{-2}_{11/2}$, because the level crossing appears between the levels $1g_{7/2}$ and $2d_{5/2}$, and the Routhians curve is not complete for $\hbar\Omega > 0.40$ MeV and $\pi h^2_{11/2} \otimes \nu h^{-2}_{11/2}$. This leads to the solution RMF-1 (the first minimum of the Routhians) with the configuration $\pi h^2_{11/2} \otimes \nu h^{-2}_{11/2}$ showing increasing values for $B(M1)/B(E2)$, as also seen in Fig. 12.

V. CONCLUSIONS

Summarizing, we have applied in this investigation the relativistic tilted axis cranking model for a fully self-consistent

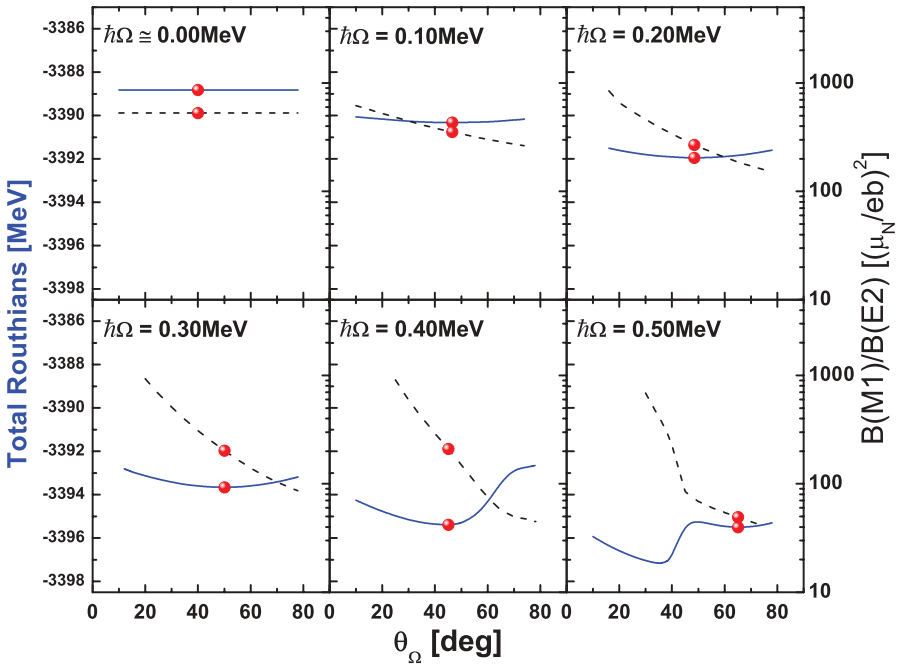

FIG. 13. (Color online) Total Routhians (solid blue line, left scale) and ratios of $B(M1)/B(E2)$ value (dashed black line, right scale) as functions of θ_Ω for various rotational frequencies $\hbar\Omega$. The solid red dots correspond to the self-consistent angle θ_{self} on both curves.

description of magnetic dipole bands. A new code for the solution of the corresponding equations has been developed. It fixes the directions of the principal axes of the density distribution along the x, y, and z axes by a quadratic constraint, and it allows for rotations with arbitrary orientation of the angular velocity $\mathbf{\Omega}$ in the xz plane (two-dimensional cranking). The invariance of space reflection $\mathcal{P}$ and the combination of the time reversal and reflection in the y direction ($\mathcal{P}_y\mathcal{T}$) are used. Based on this new tilted axis cranking RMF code, the magnetic rotation in band DB1 of the nucleus ^{142}Gd is studied with the parameter set PK1.

To save computer time, first the cranking axis is frozen at a tilted angle $\theta_\Omega = 45^\circ$, and afterward this orientation is determined in a self-consistent way by minimizing the total Routhian. In all cases, we consider at the band head ($\Omega = 0$) the configuration $\pi h_{11/2}^2 \otimes \nu h_{11/2}^{-2}$. Self-consistency requires that the orientation of the proton spin is orthogonal to that of the neutron spin at $\Omega = 0$. With increasing angular velocity, the angle between these two configurations decreases in a self-consistent way. This means we observe in band DB1 of the nucleus ^{142}Gd a shears mechanism, the characteristic of magnetic rotation. For large Ω values we find a level crossing, which leads to a rotation with the configuration $\pi[h_{11/2}^2 g_{7/2}^{-1} d_{5/2}^1] \otimes \nu h_{11/2}^{-2}$ above $\hbar\Omega > 0.4$ MeV. Before the band crossing region, i.e., for $\hbar\Omega \leqslant 0.40$ MeV, the experimental relation between the total angular momenta and the rotational frequency is well reproduced by the tilted axis cranking RMF calculation. The characteristic of magnetic rotation and the shears mechanism for DB1 in ^{142}Gd are microscopically and self-consistently demonstrated by the orientation of proton and neutron angular momenta.

Compared to the nonrelativistic Skyrme-Hartree-Fock results, in these relativistic tilted axis cranking calculations, the energies of band DB1 in ^{142}Gd as functions of the total angular momentum are in much better agreement with the experimental values.

For band DB1 in ^{142}Gd, it is demonstrated that the characteristic features of magnetic rotation can be well described by relativistic mean field theory based on tilted axis cranking, in particular the energy spectra, the relation between the total angular momenta and the rotational frequency, the shears mechanism, and the electromagnetic transition ratios $B(M1)/B(E2)$. Instead of the empirical formula used in the previous RMF calculation, the ratio $B(M1)/B(E2)$ is obtained by adopting Eq. (18) to get the nuclear magnetic moment from the nuclear current. The calculated results show the characteristic of the magnetic rotation. Future experiment is welcome in lower spin regions to validate our prediction.

ACKNOWLEDGMENTS

This work is partly supported by the Major State Basic Research Development Program under Contract No. 2007CB815000, the National Natural Science Foundation of China under Grant Nos. 10705004, 10435010, 10221003, 10505002, the Gottlieb Daimler- and Karl Benz Foundation Grants for Ph.D. Students of Peking University under Registration No. 17-05/04, the European Union project Asia-Europe Link in Nuclear Physics and Astrophysics, CN/ASIA-LINK/008(94791), the Bundesministerium für Bildung und Forschung, Germany, under Project 06MT 246, and the DFG cluster of excellence "Origin and Structure of the Universe" (www.universe-cluster.de). P.R. also acknowledges support from the Ministerio de Educación y Ciencia, Spain, under No. SAB2005-0025.

[1] B. R. Mottelson and J. G. Valatin, Phys. Rev. Lett. **5**, 511 (1960).
[2] A. Johnson, H. Ryde, and J. Sztarkier, Phys. Lett. **B34**, 605 (1971).
[3] F. S. Stephens and R. S. Simon, Nucl. Phys. **A183**, 257 (1972).
[4] B. Banerjee, H. J. Mang, and P. Ring, Nucl. Phys. **A215**, 366 (1973).
[5] J. O. Newton, B. Herskind, R. M. Diamond, E. L. Dines, J. E. Draper, K. H. Lindenberger, C. Schuck, S. Shih, and F. S. Stephens, Phys. Rev. Lett. **46**, 1383 (1981).
[6] P. J. Twin, B. M. Nyakó, A. H. Nelson, J. Simpson, M. A. Bentley, H. W. Cranmer-Gordon, P. D. Forsyth, D. Howe, A. R. Mokhtar, J. D. Morrison, J. F. Sharpey-Schafer, and G. Sletten, Phys. Rev. Lett. **57**, 811 (1986).
[7] S. Frauendorf, J. Meng, and J. Reif, in *Proceedings of the Conference on Physics From Large γ-Ray Detector Arrays*, Vol. II of Report LBL35687, edited by M. A. Deleplanque (Univ. of California, Berkeley, 1994), p. 52.
[8] A. Bohr and B. Mottelson, *Nuclear Structure* (Benjamin, Reading, MA, 1975), Vol. II.
[9] S. Frauendorf and J. Meng, Nucl. Phys. **A617**, 131 (1997).
[10] D. R. Inglis, Phys. Rev. **96**, 1059 (1954).
[11] E. Caurier, J. L. Egido, G. Martinez-Pinedo, A. Poves, J. Retamosa, L. M. Robledo, and A. P. Zuker, Phys. Rev. Lett. **75**, 2466 (1995).
[12] R. Beck, H. J. Mang, and P. Ring, Z. Phys. **231**, 26 (1970).
[13] P. Ring, R. Beck, and H. J. Mang, Z. Phys. **231**, 10 (1970).
[14] C. G. Andersson, S. E. Larson, G. Leander, P. Møller, S. G. Nilsson, I. Ragnarsson, S. Åberg, R. Bengtsson, J. Dudek, B. Nerlo-Pomorska, K. Pomorski, and Z. Szymaski, Nucl. Phys. **A268**, 205 (1976).
[15] P. Bonche, H. Flocard, and P.-H. Heenen, Nucl. Phys. **A467**, 115 (1987).
[16] J. L. Egido and L. M. Robledo, Phys. Rev. Lett. **70**, 2876 (1993).
[17] A. V. Afanasjev, J. König, and P. Ring, Nucl. Phys. **A608**, 107 (1996).
[18] A. V. Afanasjev, J. König, and P. Ring, Phys. Rev. C **60**, 051303(R) (1999).
[19] G. Baldsiefen, H. Hübel, and F. Azaiez *et al.*, Z. Phys. A **343**, 245 (1992).
[20] A. Kuhnert, M. A. Stoyer, and J. A. Becker *et al.*, Phys. Rev. C **46**, 133 (1992).
[21] R. M. Clark, R. Wadsworth, and E. S. Paul *et al.*, Z. Phys. A **342**, 371 (1992).
[22] R. M. Clark, R. Wadsworth, and E. S. Paul *et al.*, Phys. Lett. **B275**, 252 (1992).
[23] G. Baldsiefen, H. Hübel, and D. Mehta *et al.*, Phys. Lett. **B275**, 247 (1992).

[24] G. Baldsiefen, H. Hübel, and W. Korton *et al.*, Nucl. Phys. **A574**, 521 (1994).
[25] M. Neffgen, G. Baldsiefen, and S. Frauendorf *et al.*, Nucl. Phys. **A595**, 499 (1995).
[26] G. Baldsiefen, M. A. Stoyer, and J. A. Cizewki *et al.*, Phys. Rev. C **54**, 1106 (1996).
[27] R. M. Clark, S. J. Asztalos, and G. Baldsiefen *et al.*, Phys. Rev. Lett. **78**, 1868 (1997).
[28] H. Hübel, Prog. Part. Nucl. Phys. **38**, 89 (1997).
[29] S. Frauendorf, Nucl. Phys. **A557**, 259c (1993).
[30] P. Ring and P. Schuck, *The Nuclear Many-Body Problem* (Springer, Heidelberg, 1980).
[31] A. K. Jain, A. K. Jain, and B. Singh, At. Data Nucl. Data Tables **74**, 283 (2000).
[32] A. K. Kerman and N. Onishi, Nucl. Phys. **A361**, 179 (1981).
[33] H. Frisk and R. Bengtsson, Phys. Lett. **B196**, 14 (1987).
[34] S. Frauendorf and J. Meng, Z. Phys. A **356**, 263 (1996).
[35] J. Peng, J. Meng, and S. Q. Zhang, Phys. Rev. C **68**, 044324 (2003).
[36] T. Koike, K. Starosta, and I. Hamamoto, Phys. Rev. Lett. **93**, 172502 (2004).
[37] H. Madokoro, J. Meng, M. Matsuzaki, and S. Yamaji, Phys. Rev. C **62**, 061301(R) (2000).
[38] P. Olbratowski, J. Dobaczewski, and J. Dudek *et al.*, Acta Phys. Pol. B **33**, 389 (2002).
[39] P. Olbratowski, J. Dobaczewski, J. Dudek, and W. Płóciennik, Phys. Rev. Lett. **93**, 052501 (2004).
[40] J. D. Walecka, Ann. Phys. (NY) **83**, 491 (1974).
[41] B. D. Serot and J. D. Walecka, Adv. Nucl. Phys. **16**, 1 (1986).
[42] J. Boguta and A. R. Bodmer, Nucl. Phys. **A292**, 413 (1977).
[43] *Extended Density Functionals in Nuclear Structure Physics*, Lecture Notes in Physics, edited by G. A. Lalazissis, P. Ring, and D. Vretenar (Springer, Heidelberg, 2004), Vol. 641.
[44] H. Kucharek and P. Ring, Z. Phys. A **339**, 23 (1991).
[45] T. Gonzales-Llarena, J. L. Egido, G. A. Lalazissis, and P. Ring, Phys. Lett. **B379**, 13 (1996).
[46] J. Meng, Nucl. Phys. **A635**, 3 (1998).
[47] M. Serra and P. Ring, Phys. Rev. C **65**, 064324 (2002).
[48] P.-G. Reinhard, Rep. Prog. Phys. **52**, 439 (1989).
[49] P. Ring, Prog. Part. Nucl. Phys. **37**, 193 (1996).
[50] B. D. Serot and J. D. Walecka, Int. J. Mod. Phys. E **6**, 515 (1997).
[51] M. Bender, P.-H. Heenen, and P.-G. Reinhard, Rev. Mod. Phys. **75**, 121 (2003).
[52] D. Vretenar, A. V. Afanasjev, G. A. Lalazissis, and P. Ring, Phys. Rep. **409**, 101 (2005).
[53] J. Meng, H. Toki, S.-G. Zhou, S.-Q. Zhang, W.-H. Long, and L.-S. Geng, Prog. Part. Nucl. Phys. **57**, 470 (2006).
[54] Y. K. Gambhir, P. Ring, and A. Thimet, Ann. Phys. (NY) **198**, 132 (1990).
[55] G. A. Lalazissis, D. Vretenar, and P. Ring, Eur. Phys. J. A **22**, 37 (2004).
[56] G. A. Lalazissis, M. M. Sharma, P. Ring, and Y. K. Gambhir, Nucl. Phys. **A608**, 202 (1996).
[57] T. Bürvenich, M. Bender, J. A. Maruhn, and P.-G. Reinhard, Phys. Rev. C **69**, 014307 (2004).
[58] J. Meng and P. Ring, Phys. Rev. Lett. **77**, 3963 (1996).
[59] J. Meng and P. Ring, Phys. Rev. Lett. **80**, 460 (1998).
[60] G. A. Lalazissis, D. Vretenar, and P. Ring, Phys. Rev. C **69**, 017301 (2004).
[61] G. A. Lalazissis, D. Vretenar, and P. Ring, Nucl. Phys. **A650**, 133 (1999).
[62] A. Arima, M. Harvey, and K. Shimizu, Phys. Lett. **B30**, 517 (1969).
[63] K. T. Hecht and A. Alder, Nucl. Phys. **A137**, 129 (1969).
[64] J. N. Ginocchio, Phys. Rev. Lett. **78**, 436 (1997).
[65] J. Meng, K. Sugawara-Tanabe, S. Yamaji, P. Ring, and A. Arima, Phys. Rev. C **58**, R628 (1998).
[66] J. Meng, K. Sugawara-Tanabe, S. Yamaji, and A. Arima, Phys. Rev. C **59**, 154 (1999).
[67] T. Chen, H. Lu, and J. Meng *et al.*, Chin. Phys. Lett. **20**, 358 (2003).
[68] J. N. Ginocchio, Phys. Rep. **414**, 165 (2005).
[69] W. H. Long, H. Sagawa, J. Meng, and N. Van Giai, Phys. Lett. **B639**, 242 (2006).
[70] P. Ring, Z.-Y. Ma, N. Van Giai, D. Vretenar, A. Wandelt, and L.-G. Cao, Nucl. Phys. **A694**, 249 (2001).
[71] N. Paar, P. Ring, T. Nikšić, and D. Vretenar, Phys. Rev. C **67**, 034312 (2003).
[72] N. Paar, T. Nikšić, D. Vretenar, and P. Ring, Phys. Rev. C **69**, 054303 (2004).
[73] A. Ansari, Phys. Lett. **B623**, 37 (2005).
[74] A. Ansari and P. Ring, Phys. Rev. C **74**, 054313 (2006).
[75] D. Pena, Ph.D. thesis, Technische Universität München, 2007.
[76] W. Koepf and P. Ring, Nucl. Phys. **A511**, 279 (1990).
[77] J. König and P. Ring, Phys. Rev. Lett. **71**, 3079 (1993).
[78] J. Meng, J. Peng, S.-Q. Zhang, and S.-G. Zhou, Phys. Rev. C **73**, 037303 (2006).
[79] W. Koepf and P. Ring, Nucl. Phys. **A493**, 61 (1989).
[80] A. R. Edmonds, *Angular Momentum in Quantum Mechanics* (Princeton University, Princeton, NJ, 1957).
[81] J. M. Yao, H. Chen, and J. Meng, Phys. Rev. C **74**, 024307 (2006).
[82] M. Abramowitz and I. A. Stegun, *Handbook of Mathematical Functions* (Dover, New York, 1965).
[83] G. A. Leander and R. K. Sheline, Nucl. Phys. **A413**, 375 (1984).
[84] A. L. Goodman, Nucl. Phys. **A230**, 466 (1974).
[85] M. Girod and B. Grammaticos, Phys. Rev. C **27**, 2317 (1983).
[86] D. Vautherin, Phys. Rev. C **7**, 296 (1973).
[87] Y. K. Gambhir and P. Ring, Mod. Phys. Lett. A **8**, 787 (1993).
[88] W. Long, J. Meng, N. Van Giai, and S.-G. Zhou, Phys. Rev. C **69**, 034319 (2004).
[89] R. R. Chasman and S. Wahlborn, Nucl. Phys. **A90**, 401 (1967).
[90] J. D. Talman, Nucl. Phys. **A141**, 273 (1970).
[91] B. Simon, Phys. Rev. Lett. **51**, 2167 (1983).
[92] T. Bengtsson, Nucl. Phys. **A496**, 56 (1989).
[93] R. M. Lieder, T. Rzaca-Urban, and H. Brands *et al.*, Eur. Phys. J. A **13**, 297 (2002).
[94] A. A. Pasternak, E. O. Podsvirova, and R. M. Lieder *et al.*, Eur. Phys. J. A **23**, 191 (2005).
[95] P. Olbratowski, Ph.D., thesis, University of Warsaw, 2004.
[96] I. Hamamoto, Nucl. Phys. **A271**, 15 (1976).
[97] J. L. Egido, H. J. Mang, and P. Ring, Nucl. Phys. **A334**, 1 (1980).